nature communications

Article

https://doi.org/10.1038/s41467-025-59458-y

Structural proteomics defines a sequential priming mechanism for the progesterone receptor

Received: 30 October 2024

Accepted: 24 April 2025

Published online: 12 May 2025

Check for updates

Matthew D. Mann[1,2], Min Wang[3], Josephine C. Ferreon[4], Phoebe S. Tsoi[4], Michael P. Suess[3], Antrix Jain[5], Anna Malovannaya[4], Roberto Vera Alvarez[6], Bruce D. Pascal[6], Raj Kumar[7], Dean P. Edwards[3] & Patrick R. Griffin[1,2]

The progesterone receptor (PR) is a steroid-responsive nuclear receptor with two isoforms: PR-A and PR-B. Disruption of PR-A:PR-B signaling is associated with breast cancer through interactions with oncogenic co-regulatory proteins (CoRs). However, molecular details of isoform-specific PR-CoR interactions remain poorly understood. Using structural mass spectrometry, we investigate the sequential binding mechanism of purified full-length PR and intact CoRs, steroid receptor coactivator 3 (SRC3) and p300, as complexes on target DNA. Our findings reveal selective CoR NR-box binding by PR and unique interaction surfaces between PR and CoRs during complex assembly, providing a structural basis for CoR sequential binding on PR. Antagonist-bound PR showed persistent CoR interactions, challenging the classical model of nuclear receptor activation and repression. In this work, we offer a peptide-level perspective on the organization of the PR transcriptional complex and infer the mechanisms behind the interactions of these proteins, both in active and inactive conformations.

The progesterone receptor (PR) is a steroid-activated nuclear receptor and belongs to the subfamily of steroid hormone receptors (SRs) that includes the estrogen receptor, androgen receptor, mineralocorticoid receptor, and glucocorticoid receptor. SRs, including PR, are ligand-dependent transcriptional regulatory proteins that exhibit remarkable functional diversity in mediating cell/tissue and target gene-specific responses, largely driven by conformational dynamics of the protein that enables its binding to DNA response elements and unique subsets of transcriptional co-regulatory proteins (CoRs). Like other SRs, PR is a modular protein composed of well-folded ligand binding (LBD) and DNA binding (DBD) domains that are connected via a structurally dynamic hinge region, and an intrinsically disordered (ID) N-terminal domain (NTD). The hinge, additionally termed carboxyl terminal extension (CTE), is more than a flexible linker. It forms an extended loop that interacts with the minor groove of DNA flanking either side of inverted repeat progesterone response element DNA (PRE) to extend the protein-DNA interface beyond that of the core DBD that binds the major groove of PREs[1,2]. PR also contains dimerization domains, one within the LBD and another DNA-binding dependent dimerization domain in the DBD. Similar to other SRs, PR also contains transcriptional activation functions (AFs), a ligand-independent AF1 in the NTD and ligand-dependent AF2 in the LBD, that provide interaction surfaces for CoRs[3–5].

[1]Skaggs Graduate School of Chemical and Biological Sciences, Scripps Research, La Jolla, CA, USA. [2]Department of Molecular Medicine, The Herbert Wertheim UF Scripps Institute for Biomedical Innovation & Technology, Jupiter, FL, USA. [3]Department of Molecular and Cellular Biology, Baylor College of Medicine, Houston, TX, USA. [4]Verna and Marrs McLean Department of Biochemistry and Molecular Pharmacology, Baylor College of Medicine, Houston, TX, USA. [5]Mass Spectrometry Proteomics Core Facility. Advanced Technology Cores, Baylor College of Medicine, Houston, TX, USA. [6]Omics Informatics LLC, Honolulu, HI, USA. [7]Department of Pharmaceutical and Biomedical Sciences, Touro College of Pharmacy, Touro University, New York, NY, USA.
e-mail: pgriffin2@ufl.edu

The primary physiological role of progesterone, acting through PR, is to regulate the development, differentiation, and functional maintenance of female reproductive tissues and the endocrine hypothalamic-pituitary-ovarian axis. In addition to expression in major target tissues such as the mammary gland, uterus, ovary, and brain, PR is expressed in a variety of other tissues, including the pancreas, bone, lung, heart, adrenal gland, liver, kidney, prostate, and tissues of the lower urinary tract, and thus can exert biological actions in a variety of other organs throughout the body[6–18]. PR is also expressed in breast and uterine cancers and other endocrine disorders, such as endometriosis, mediating pathophysiological effects of progesterone in these systems[19]. There are two protein isoforms of PR, PR-A and PR-B, that are expressed through alternate utilization of two promoters, and are transcripts of the same gene, reviewed here[3,4,20]. PR-A is an N-terminal truncation (missing aa 1-164) compared to full-length PR-B, and is generally a weaker transcriptional activator than PR-B due to the presence of a strong transcriptional activation function (AF3) within the extended NTD, unique to PR-B[21]. PR-A also has a trans repressor function over other SRs[22]. The ratios of PR-A to PR-B expression vary widely, dependent on target tissue and physiological conditions. Differential expression of PR-A and PR-B occurs during developmental stages of the mammary gland[23] and in different cell and tissue compartments of the uterus during development and the menstrual cycle[24–27]. PR-B is dominant in the hypothalamus, while PR-A is the major isoform in the pituitary[28], and PR-B is reported to be the most abundant isoform in many non-endocrine tissues[12]. Many breast cancers express both PR isoforms, but in some tumors, the ratios are altered with overabundance of one isoform over the other[23,29–34]. Specifically in endometriosis, PR-A expression is dominant over PR-B[35]. Distinct physiological roles for PR isoforms have been shown by tissue and PR isoform-specific knockout studies in mice, which revealed that PR-B is the functionally more important isoform for mammary gland development[13] while PR-A is more important in the uterus and ovary[3,4]. As separately expressed proteins, PR-A and PR-B have been shown by gene microarray and RNA-seq to regulate a common as well as distinct set of genes, to have overlapping as well as distinct chromatin binding sites (cistromes) as assessed by ChiP-Seq, and to recruit different as well as shared sets of cofactors[28,36,37]. Interestingly, PR isoform-specific cistromes are enriched with the same consensus PRE binding motifs, indicating that PR-A and PR-B are recruited differently to genomic sites. In the absence of ligand, PR-A is localized primarily in the nucleus, while PR-B is distributed between the cytoplasm and nucleus and undergoes nuclear translocation in response to binding hormone[38,39]. PR has multiple nuclear localization sequences (NLS), suggesting they are not equivalently accessible in the two PR isoforms due to distinct conformations or unique interacting co-factors[38]. This differential intracellular localization contributes to rapid extra-nuclear progesterone activation of cell signaling protein phosphorylation pathways independent of transcriptional activity that is mediated by PR-B only and not by PR-A[39].

The mechanistic basis for the different biological actions of PR isoforms is not well understood. It is generally believed that a major contributing factor is distinct structure conformations in the PR-A and PR-B that provide unique interaction surfaces for various co-regulatory proteins. This remains a largely unresolved question, due to a lack of high-resolution structures of full-length SRs and CoRs. High-resolution crystal structures have been determined for the PR DBD-CTE[1] complexed with a consensus inverted repeat palindromic PRE DNA, and the PR LBD complexed with a progesterone agonist[40] or antagonist-bound with a peptide from a transcriptional co-repressor[41,42]. However, the conformational flexibility of full-length SRs and CoRs due to large regions of intrinsic disorder, coupled with their large sizes and multiple domains, makes them unsuitable for either high-resolution NMR or X-ray crystallography analysis. Recent CryoEM studies of a PR-B:SRC2:p300/DNA complex assembled with all full-length proteins were reported, but lower-resolution structures were unable to provide details of specific interactions of PR with CoRs at the atomic level, presumably due to high conformational flexibility[43].

As an alternative to classical structural techniques, we present here a structural proteomics approach to obtain amino acid level resolution of protein interactions and conformational changes in assembled complexes, containing full-length PRs and known CoRs, steroid receptor coactivator 3 (SRC3), and the histone acetyltransferase p300[43–45]. One approach, Hydrogen-deuterium exchange (HDX) mass spectrometry (MS), works on the principle of backbone amide exchange, where protein backbone amide hydrogens will freely exchange to deuterium upon regular protein motion[46–50]. This is a useful technique where differential deuterium exchange informs protein conformational changes and protein-protein interaction sites. Crosslinking (XL) coupled MS provides additional information on amino acid proximity, which is useful in determining protein-protein interaction regions[51–54]. Through a combination of HDX-MS and XL-MS, we present a higher-resolution structural understanding of the organization of the PR ternary complex compared to available structures. To date—and to our knowledge—this is the highest resolution structural data generated for full-length PR and CoRs through the utilization of structural mass spectrometry techniques. These studies differ from prior ones due to the complexity of full-length PR and CoRs, while informing interprotein amino acid proximity and amide backbone interactions.

Results herein provide insights into interaction surfaces between PR and SRC3 and p300 during complex assembly with and without DNA that may contribute to distinct functional activities of PR isoforms. Our data suggests a sequential binding mechanism that gives an order to PR binding CoRs. Further, structural proteomic information is garnered for PR in complex with a progestin antagonist, revealing continued interactions between PR and both co-activators in an altered manner as compared to the active PR-agonist complex. Most likely to be applicable to the other steroid hormone receptors, our insights into PR-CoR dynamics and interaction surfaces explore potential mechanisms by which receptors bind to DNA/chromatin and build their respective activation complexes for transcriptional responses.

Results

Strep-II tagged recombinant PR and CoRs generates stable protein and complexes

Intact full-length PR and CoRs were expressed and purified as recombinant proteins in *Spodoptera frugiperda (Sf9)* insect cells using the baculovirus system[55]. This is an ideal expression system for full-length PR, shown previously to retain native folding and post-translational modifications, including phosphorylation on the same sites as occurs with endogenous PR in mammalian cell types[56,57]. In addition, purified full-length PR from the baculovirus system was previously demonstrated to exhibit stoichiometric ligand binding activity, high affinity binding to PRE DNA, including free DNA and when assembled on nucleosomes, and transcriptional activity in cell-free assays[55,58–61]. As an improvement upon previous methods for expression and purification of PR, a Strep-II affinity tag at the N-terminus of PR was used in place of poly-histidine[57,62].

Strep-II is a minimal eight-amino-acid peptide that binds to the core of streptavidin and has superior properties for efficient affinity purification of recombinant fusion proteins. Since the Strep-II tag is biologically inert and does not affect protein folding, it is potentially ideal for the isolation of large multi-domain proteins like PR and CoRs in their intact native state[63]. Strep II-tagged PR-A or PR-B were expressed in *Sf9* insect cells in the presence of the synthetic progestin agonist R5020 to bind and stabilize the receptor in an active conformation in culture. As described in more detail in Methods, receptors in native cell lysates were purified through two-step affinity and size-

exclusion chromatography (SEC). The SEC fractions from the major protein peak that correspond with the expected molecular size of monomeric PR were pooled and concentrated in the range of 1.5 to 1.6 mg/ml (15–18 μM) with yields between 2.25 to 2.4 mg of total purified protein from 1 liter of *Sf9* cell cultures. Assessed by SDS-PAGE, each purified PR isoform contained a single major protein band of expected molecule size with a purity >98% (Supplementary Fig. 1). Yields were higher than with poly-histidine tagged PR from previous work, presumably due to the greater efficiency of Strep II tagged affinity system that results in fewer contaminating proteins with a single purification step. Mass spectrometry confirmed the identity of major SDS-PAGE protein bands of purified PR-A and PR-B as intact full-length PR-A or PR-B with no other peptides identified from unrelated insect cell protein background with a coverage > 89% (Supplementary Fig. 2). A minor protein band of ~ 3 kDa faster mobility on SDS-PAGE than the major intact PR was observed after the first affinity purification step with either PR isoform (Supplementary Fig. 1). Further mass spectrometry analysis of this protein band showed it is largely full-length PR, as opposed to an unrelated contaminant or truncated PR, but with a different pattern of phosphorylation as compared to the major slower mobility protein band (Supplementary Fig. 3A, B). PR is phosphorylated on multiple serine residues, and previous work has shown that phosphorylation of specific sets of sites produces an upshift of mobility on SDS-PAGE larger than the molecular mass of the phosphate moieties[56,64]. Phosphorylation-dependent induced structural changes that produce anomalous migration on SDS gels has been commonly observed and determined to be due to reduced binding of SDS to negatively charged phosphoamino acids[65].

CoRs, SRC3, and p300 were expressed in *Sf9* insect cells and purified in a similar two-step procedure as full-length constructs with Strep II affinity tags. This resulted in SRC3 (Supplementary Fig. 4) and p300 (Supplementary Fig. 5) exhibiting singular major bands on SDS-PAGE of expected molecular size at greater than 98% purity. The concentrations of purified SRC3 and p300 were in the range of 2.0-2.5 mg/ml (12uM and 9uM) with yields of 2.0–2.5 total mg from 1 liter of *Sf9* cell cultures. Mass spectrometry confirmed the identity of SRC3 and p300, each as intact full-length protein with no detectable unrelated insect cell peptides (Supplementary Fig. 6).

Quality of purified proteins and DNA-induced dimerization of PR

As a further assessment of the quality of purified proteins, we performed Microfluidic Modulation Spectroscopy (MMS) using an Aurora TX RedShift Biosystem. MMS is an automated infrared (IR) spectroscopy technology for sensitive and accurate measurement of the secondary structure of proteins. Differential absorption profiles with Gaussian curve fitting was used to determine the signal contribution from distinct secondary structures or unordered regions[66,67]. The calculated higher ordered structures (HOS) for each protein (PR-A, PR-B, SRC3 and p300) by this analysis gave percentages of beta sheet, alpha helix, beta turn and unordered structure similar to the predicted fractional secondary and unordered structure from the protein data base and by AlphaFold (Supplementary Fig. 7). These MMS results indicate that purified full-length PR and co-regulatory proteins are in native folded states.

Size-exclusion chromatography-multi-angle light scattering (SEC-MALS) analysis was performed for each purified protein alone and with assembled protein-DNA complexes. This is an analytical technology capable of determining accurate molecular weights of proteins or multi-protein complexes under native conditions[68]. SEC-MALS chromatograms for each individual protein displayed single, homogenous peaks with experimentally derived molecular weights (MW) within the expected theoretical MW for each macromolecule as a monomer, except PR-B, which behaved as a mixture of monomer and dimer (Fig. 1, Supplementary Fig. 8, and Supplementary Table 1). Slight discrepancies between experimental and theoretical MWs of individual proteins are likely due to deviation of dn/dc values from that of BSA, used as a standard. BSA is a globular protein, while PR, SRC3, and p300 have significant disordered regions. In the absence of DNA, PR-A, liganded to the progestin agonist R5020, gave an experimentally determined MW of a protein monomer while binding to DNA, resulting in an experimentally determined MW within the expected theoretical for a PR-A dimer (Fig. 1 and Supplementary Table 1). PR-B liganded with R5020 gave a mixture of monomer and dimer MW distributions in the absence of DNA, and a single MW distribution within the expected theoretical for a PR-B dimer upon binding DNA (Fig. 1 and Supplementary Table 1). These results are consistent with previous data showing that PR forms stable dimers when complexed with a PRE. Upon addition of SRC3 to a preformed PR-A/PRE DNA complex, SEC-MALS detected a major homogenous peak of experimentally determined MW of 348.3 (+ /− 30.6) kDa with little or no detectable peaks with the sizes of SRC3 or PR-A/DNA alone. This MW is within experimental error of the theoretical of 344.8 kDa for a ternary complex with a stoichiometry of 1 SRC3:2 PR:1 DNA (Supplementary Fig. 8, Supplementary Table 1). Upon addition of p300 and SRC3 to a preformed PR-A/DNA complex, SEC-MALS measured a major single homogenous peak with a MW of 611.6 (+/− 30.6) kDa that is within experimental error of the theoretical MW of 611.8 kDa for a quaternary complex with a stoichiometry of 1 p300:1 SRC3:2 PR:1 DNA (Supplementary Fig. 8 and Supplementary Table 1). Assembly of SRC3 and p300 with the PR-B/PRE DNA complex also gave experimental MWs within the theoretical for PR-B ternary and quaternary complexes with the same stoichiometries as the PR-A complex. SEC-MALS data demonstrate the ability of full-length purified PR and CoRs to assemble as stable complexes under these experimental conditions and are consistent with a stoichiometry of 1:1:2:1 (p300:SRC3:PR:DNA) in the complex, agreeing with the PR:SRC2:p300/DNA CryoEM structure previously reported[43].

DNA binding induces PR isoform specific conformational changes

Hydrogen-deuterium exchange mass spectrometry (HDX-MS) was used initially to examine the effect of DNA binding on PR conformation. The deuterium exchange of non-DNA-bound PR-A and PR-B were compared to ensure similar deuterium exchange profiles for the buffers used. Each isoform showed similar exchange profiles, demonstrating that any effects of DNA on solvent exchange are not due to intrinsic differences between PR isoforms (Supplementary Fig. 9). Perturbations in deuterium exchange induced by DNA binding differ between the PR-A/PRE and PR-B/PRE complexes (Fig. 2A). Addition of PRE DNA resulted in decreased deuterium exchange throughout the PR-A DBD and LBD, indicating DNA-mediated stabilization of these domains (Fig. 2A, B). Overlaying these results on an AlphaFold model, generated using the AF3 web server[69], of the PR DBD-CTE-LBD complexed with PRE DNA shows that the regions of decreased solvent exchange correspond to dimerization domain regions or those that interface with the PRE DNA (Fig. 2B). Differential HDX-MS of PR-B revealed fewer perturbations within regions of the NTD, DBD-CTE, and LBD in response to DNA than PR-A; however, both PR-A and PR-B underwent reductions in deuterium exchange within both dimerization domains (PR-B amino acids: 602-618 and 885-922) when DNA-bound (Fig. 2A, B). Thus, alterations in deuterium exchange are likely a combination of homodimerization and DNA binding. Interestingly, decreased solvent exchange was observed in the region of the PR-B NTD common to both isoforms (amino acids 270-276), but only in PR-B and not observed for PR-A.

Crosslinking mass spectrometry (XL-MS) was used to assess amino acid proximity, which can inform inter- and intradomain interactions. The chemical crosslinker DSSO, disuccinimidyl sulfoxide, chemically crosslinks lysine residues, and XL-MS showed a rearrangement between the CTE and LBD when DNA was present,

https://doi.org/10.1038/s41467-025-59458-y

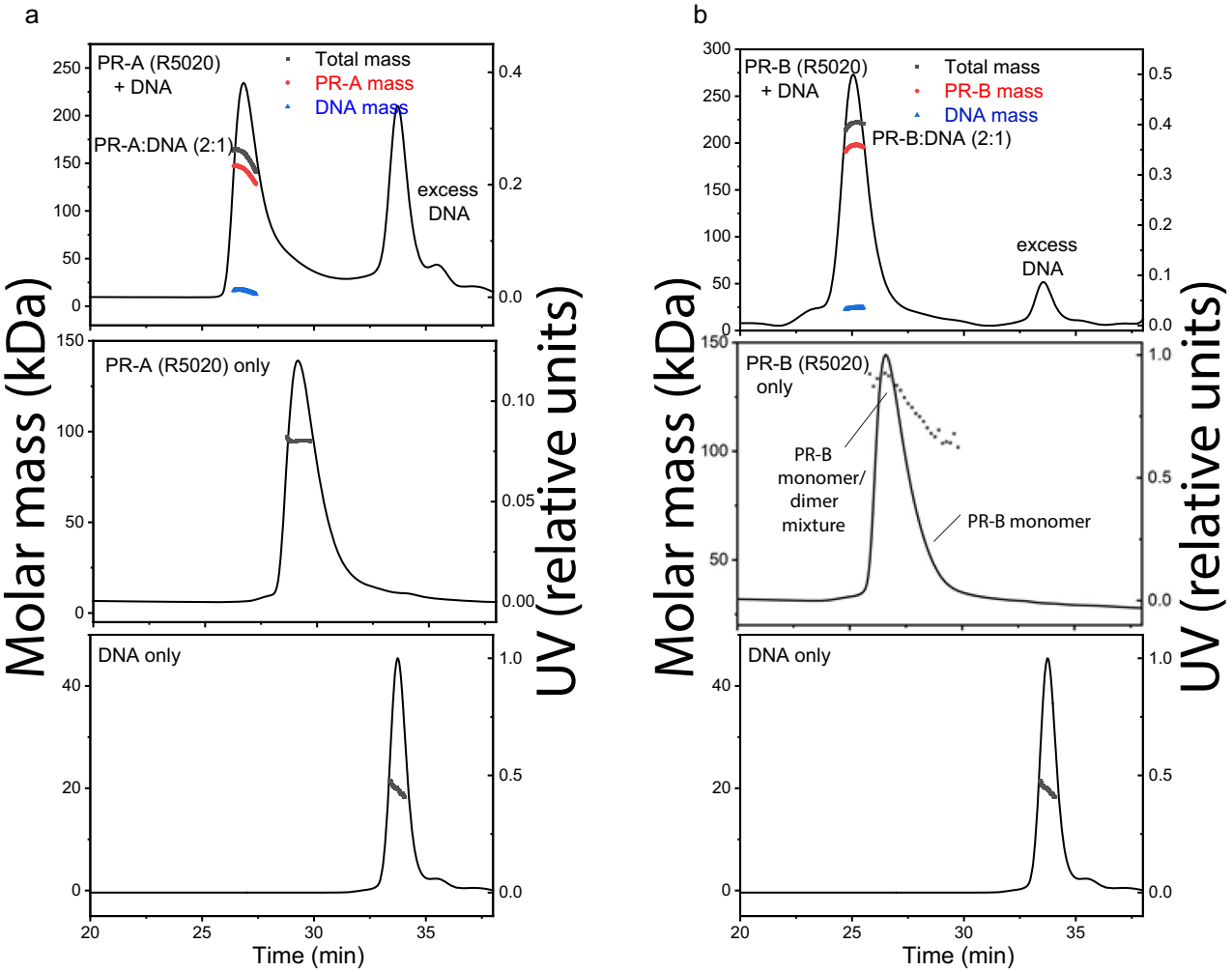

Fig. 1 | DNA induces assembly of PR-A and PR-B. a, **b** SEC-MALS chromatograms of agonist (R5020)- bound PR-A (**a**) and PR-B (**b**) with and without DNA. The molar mass of DNA and PR-A alone matches the monomeric molar mass (black line/dots across the peaks). DNA induces assembly of both PR-A and PR-B into a complex with 2:1 (protein:DNA) stoichiometry. The presence of DNA in the complexes was confirmed by deconvolution of the protein and DNA fractions in the peak (red and blue lines, respectively). Source data are provided as a Source Data file.

indicating compaction of those regions upon DNA binding (Fig. 2C, D). This was identified through a reduction in the number of crosslinks. Simultaneously, crosslinks from the PR-A N-terminus to C-terminus (residues 240 and 933) were diminished, indicating that these domains are no longer in proximity when PR is bound to DNA, most likely due to PR stabilization through homodimerization (Fig. 2C). Overall, there was a reduction in the number of enriched crosslinks in the PRE-treated sample, indicating that these lysine residues are no longer in proximity. This suggests an overall relaxation of PR upon DNA-mediated dimerization. However, this does not preclude the possibility of monomer rearrangement of this region, which remains an equally valid conclusion. The XL-MS data, taken together with the DNA-induced dimerization shown by SEC-MALS (Fig. 1), are more consistent with this change as a dimerization-driven event. Intraprotein crosslinks in PR-B between the N-terminus to C-terminus (residue 7 to 933) were also lost upon DNA binding (Fig. 2D, Red). The reduction of these N- to C-term crosslinks while other crosslinks from AF1 to AF2 regions are retained suggests a movement of the PR NTD away from the LBD. All together, these data show PR NTD stabilization through NTD-LBD interactions without DNA present. When bound to a canonical PRE, PR rearranges to shift the position of the NTD slightly away from the LBD, and these interactions are no longer required for protein stability (Fig. 2).

Co-regulator binding induces conformational changes to each PR isoform

Using a sequential strategy of assembly of PR-CoR-DNA complexes, we first examined the differential deuterium exchange for PR ± DNA compared to the differential deuterium exchange for the PR:SRC3 ± DNA complex, using the stoichiometries discerned from the PR:SRC3:PRE SEC-MALS results (2 PR:1 SRC3:1 PRE; Supplementary Fig. 8). Reductions in deuterium exchange were observed throughout PR-A (Fig. 3), indicating that SRC3 can bind and influence PR-A conformation in the absence of DNA (Fig. 3A). The SRC3-mediated reductions in deuterium exchange were not localized around one specific PR-A domain, but rather the decreased deuterium exchange was observed throughout the dimerization domains, NTD, and CTE (Fig. 3). This was analogous to the effect of DNA on PR from our HDX-MS results (Fig. 2), indicating SRC3 may facilitate PR dimerization without requiring DNA. Similar deuterium exchange reductions were observed in the PR-A NTD of PR-A complexed with SRC3 when DNA-bound, suggesting direct PR NTD and SRC3 interactions (Fig. 3B). These interactions may be necessary for stabilizing the PR:SRC3 complex to position PR in a manner amenable for DNA interactions. If this were the case, it would make sense that the PR NTD becomes rearranged both with and without DNA. Interestingly, the PR-A LBD in the PR-A:SRC3 complex showed increased deuterium exchange when

https://doi.org/10.1038/s41467-025-59458-y

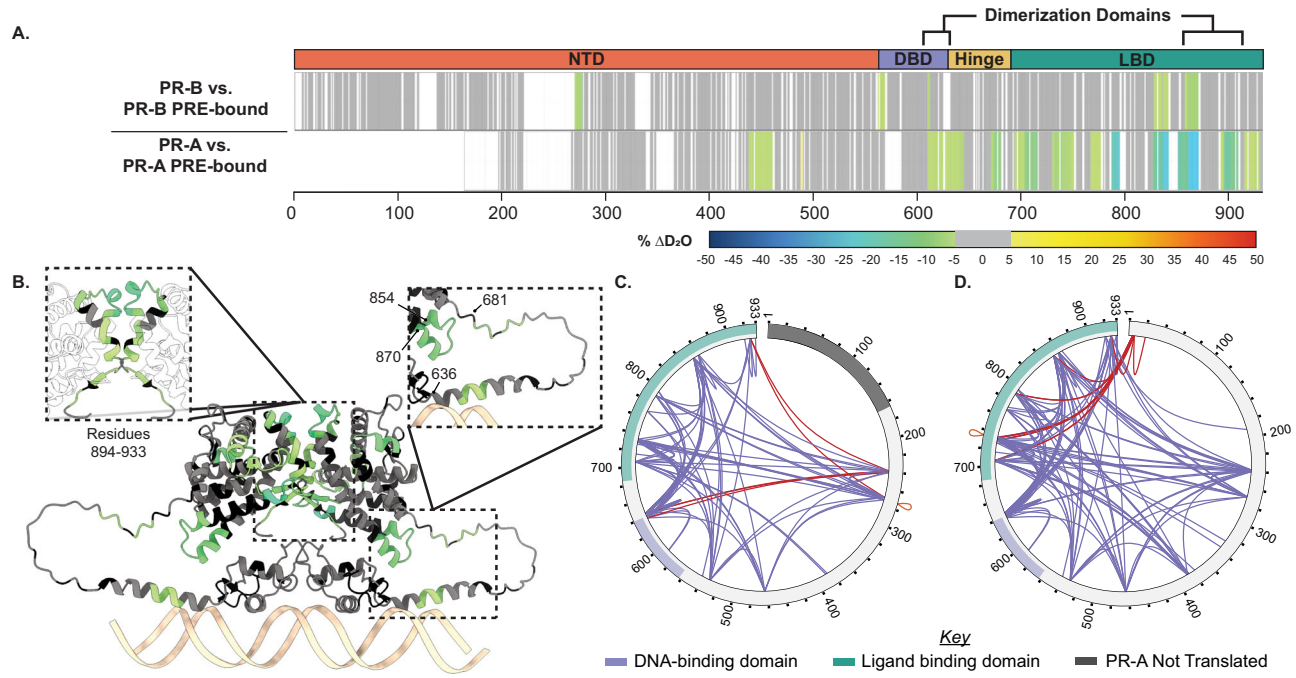

Fig. 2 | Structural proteomics reveals isoform differences upon progesterone response element (PRE) binding. A Consolidated HDX-MS data, run in triplicate, showing the differential analysis between unbound PR vs. PRE-bound, where the top is PR-B, and the bottom is PR-A. Domains are labeled as follows: N-terminal Domain (NTD), DNA-binding domain (DBD), Hinge region (Hinge), and Ligand-binding domain (LBD). Exchange data is representative of a full seven-timepoint differential HDX experiment with sample injection after 10, 30, 60, 300, 900, and 3600 s of deuterium exchange. **B** Trimmed AlphaFold 3.0 model (residues 375–769) of PR-A homodimer with unbound PR-A vs. PR-A:PRE HDX overlays. Highlighted regions are the PR dimerization domain (residues 885–922 within LBD) and the DBD C-terminal extension (right, residues 633–670). Residue labeling corresponds to the PR-B numbering. Cooler colors indicate comparative reductions in deuterium exchange. **C** XiView images of differential PR-A ± PRE experiments, where all validated crosslinks are shown. Selected N-terminal crosslinks not identified in PR-A:PRE XL-MS experiments are highlighted in red, with crosslinks mapped onto PR-B numbering, with the gray region representing the 164 amino acids not expressed in PR-A. Results representative of triplicate experiments, with validation in Skyline. **D** XiView of differential PR-B ± PRE experiments, where all validated crosslinks are shown. Selected N-terminal crosslinks not identified in PR-B:PRE XL-MS experiments are shown in red.

DNA-bound (Fig. 3B). This was unexpected, as PRE addition was expected to enhance complex stability like that observed for the PR:PRE complexes (Fig. 2). Yet even though increased exchange was observed in the LBD, neither the dimerization domains nor the AF2 region (hydrophobic pocket encompassing helices 3, 4, and 12) were affected. This indicates that the receptor binding to either PRE/DNA, SRC3, or a combination of the two influences the conformational dynamics of the PR LBD without destabilizing the homodimer.

Similar exchange profiles were observed for PR-B within an SRC3 complex (Supplementary Fig. 10). However, PR-B displayed fewer regions of differential exchange across the protein, compared to PR-A. In the PR-B:SRC3 complex, some reductions in deuterium exchange were observed in the PR-B NTD; however, not throughout the rest of the protein (Supplementary Fig. 10). DNA binding does not seem to affect the PR-B:SRC3 complex, where few differences are measured between the PR-B homodimer and PR-B:SRC3 (Supplementary Fig. 10). Taken together, these data suggest a concerted SRC3-mediated deprotection of the PR LBD and protection of the DBD-CTE when in the DNA-containing complex, and stabilization of PR when bound to SRC3 in the absence of DNA. This may indicate an SRC3-mediated PR priming mechanism, where deprotections to the solvent boundary, indicated by an increase in solvent exchange, may increase the solvent-accessible surface area for additional CoR binding.

However, to understand how the HDX results translate to protein structure, AlphaFold 3.0[69] predictions were generated for the unbound and PRE-bound PR:SRC3 complexes as a means of visualizing the HDX-MS data in 3-D space. Since AlphaFold 3.0 introduces spurious structural order (termed, hallucinations)[69] to ID regions such as the NTD of PR, 25 independent models were generated by repeating structural predictions five times with random seed values to approximate trends for the complex (Supplementary Fig. 11). The models represent potential PR-CoR binding interfaces; however, there is limited cohesion between each model due to the large ID regions in either PR or its CoRs. At best, the models show similar structural trends, but PR-CoR positioning seems to change the most between models. Thus, we sought to use our experimental HDX data to guide our model choice for HDX data visualization. These models were examined with HDXer[70] to identify the model that best fits the HDX-MS data. HDXer alone has not been validated on multi-protein ensembles. However, HDXer has been used in conjunction with MD simulations to help reweight output models. For this case, AlphaFold 3.0 models were treated as MD simulation outputs, and HDXer was used to score each of these models according to our experimental data. From the HDXer scores, we selected the best-fit model based on root mean square error (RMSE). For each top-scoring model, there was an average RMSEs of less than 0.5 (Supplementary Fig. 11). This model is not an absolute representation of each PR-CoR complex, but rather it is the best representation picked from a selection of models. The top 5 scoring HDXer models are shown in Supplementary Fig. 11 with their respective RMSEs reported.

The top model for non-DNA-bound and DNA-bound PR-A displays differing SRC3 binding modalities, where SRC3 envelops the PR-A homodimer only in the DNA-bound model (Fig. 3). The non-DNA-bound model exhibits a distinct separation between PR and SRC3, showing the main interaction site as the AF2-cleft (Fig. 3). When bound to DNA, the homodimer binds to the DNA on one face while SRC3 energetically favors binding on the opposite side of the DNA (Fig. 3).

https://doi.org/10.1038/s41467-025-59458-y

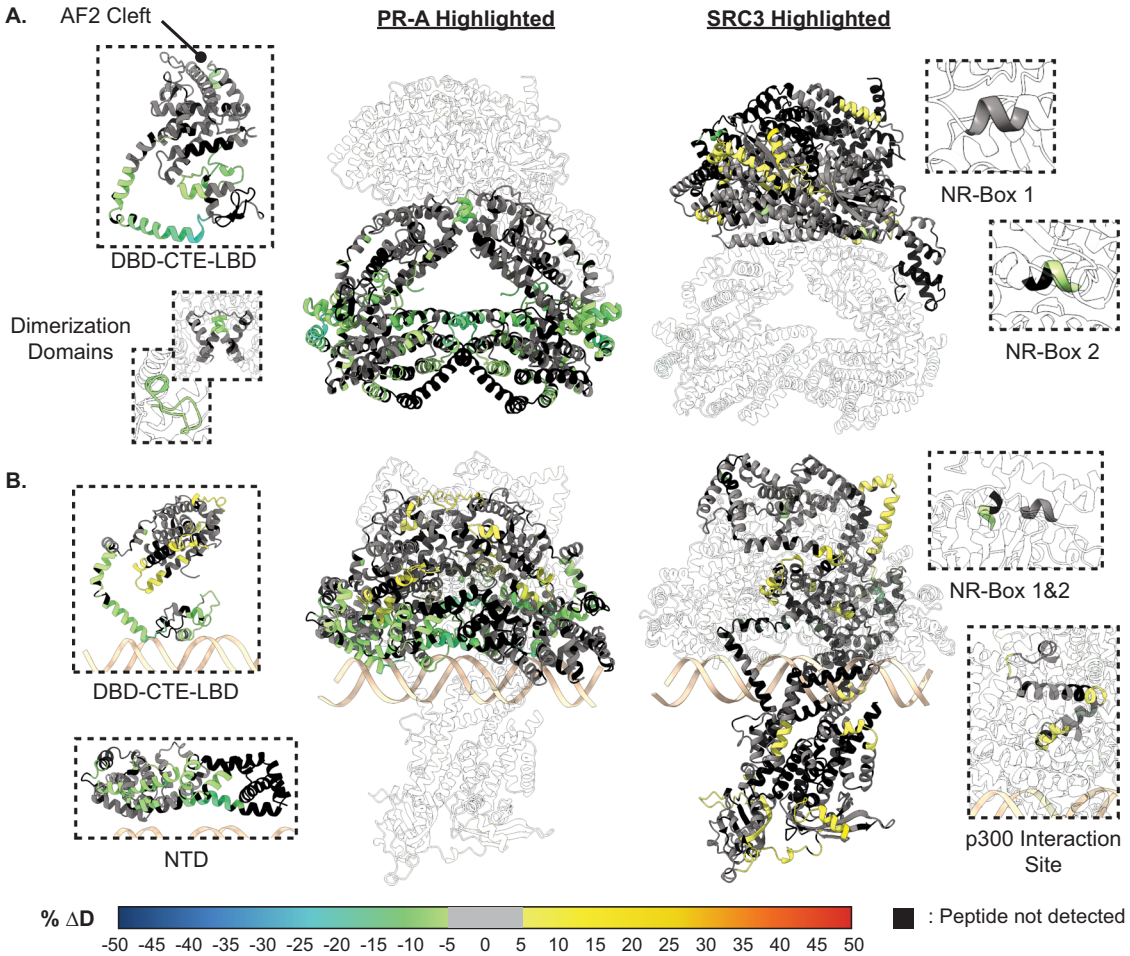

Fig. 3 | SRC3 induces LBD changes to PR upon PRE addition. A Left HDX overlay (PR-A vs. PR-A:SRC3, both non-DNA bound) mapped onto AlphaFold3.0 model of the PR-A:SRC3 ternary complex with the PR homodimer highlighted. Zoomed-in sections of PR corresponding to the dimerization domains (PR-B amino acids: 855-922 and 602-618) and N-terminal domain (PR-A amino acids 1-476) highlighted with matching HDX overlays. Right. Differential HDX overlay of SRC3 vs. PR-A:SRC3 onto the best scoring PR:SRC3 apo complex with SRC3 highlighted. NR-boxes 1 and 2 (amino acids 685-689 and 738-742, respectively) zoomed-in up to show differential exchange. **B Left**. HDX overlay (PR-A:PRE vs. PR-A:SRC3:PRE, both DNA-bound) mapped onto AlphFold3.0 model of PR-A:SRC3:PRE ternary complex with the PR homodimer highlighted. One PR-A monomer is shown as a zoomed-in section. **B Right**. Differential HDX overlay of SRC3 vs. PR-A:SRC3:PRE onto the best-scoring PR:SRC3 apo complex with SRC3 highlighted. NR-boxes 1 and 2 and the p300 interaction site (amino acids 1023-1093) are highlighted to show differential exchange. Black peptide regions correspond to peptides not identified by HDX-MS. Each color represents the percent change in deuterium incorporation (Δ%D), following the scale shown at the bottom, where darker blues correspond to decreased differential deuterium exchange and warmer reds correspond to increases in differential deuterium exchange. Exchange data is representative of a full seven-timepoint differential HDX experiment with sample injection after 10, 30, 60, 300, 900, and 3600 s of exchange time.

This was consistent throughout the top 5 scoring AlphaFold 3.0 models based on the HDX data (Supplementary Fig. 12). Overlaying the HDX data, it was clear to see that the HDX-MS data indicate a simultaneous stabilization of the DBD-CTE and increased motility at helical connecting regions, shown through the differential exchange (Fig. 3B, Left). Representative PR-B:SRC3 AlphaFold models suggest a similar binding modality to PR-A. When bound to DNA, the best fit model has PR-B adopting an elongated structure (Supplementary Fig. 10). While the orientation of SRC3 is similar between each PR isoform, PR-B has enhanced protein-protein interactions due to its extended NTD (termed AF3, Supplementary Fig. 10).

XL-MS was next used to identify intra- and interprotein interactions in PR:SRC3:DNA complexes. When non-DNA bound, PR-A showed multiple intraprotein crosslinking between N-terminal AF1 and C-terminal AF2 (Supplementary Fig. 13). Additional intraprotein crosslinks were measured in PR-B between its unique extended N-terminus and C-terminal AF2. SRC3 showed multiple interactions at PR AF2, located in the LBD, and with multiple other regions of PR (Supplementary Fig. 13). The XL-MS data indicated that there were more PR:SRC3 interactions upon DNA addition. This was seen through the additional interprotein crosslinks between PR and SRC3 in the DNA-containing samples (Supplementary Fig. 13). Moreover, increased PR intraprotein crosslinking is indicative of receptor dimerization. Adding the HDX to the crosslinking maps established that differential exchange was localized to inter- or intraprotein crosslinking regions, indicating the two methods agree (Supplementary Fig. 13). These showed that the reduction in exchange near AF2 was most likely induced by SRC3 binding, and the changes in deuterium exchange upon PRE binding aligned with PR:SRC3 interprotein crosslinks (Supplementary Fig. 13). Other regions across PR showed corroborating HDX-MS and XL-MS data, which gives greater confidence that the regions of differential deuterium exchange were SRC3-mediated.

In a similar manner to the PR:SRC3 complex, p300 was added to the transcriptional complex to assess p300 interaction sites on PR using HDX-MS and XL-MS. When p300-bound, there was more than a 10% change in deuterium exchange for both PR and SRC3, which was notable (Figs. 4, 5). More pronounced decreases in deuterium exchange show that p300 strengthens the ternary complex, whether

https://doi.org/10.1038/s41467-025-59458-y

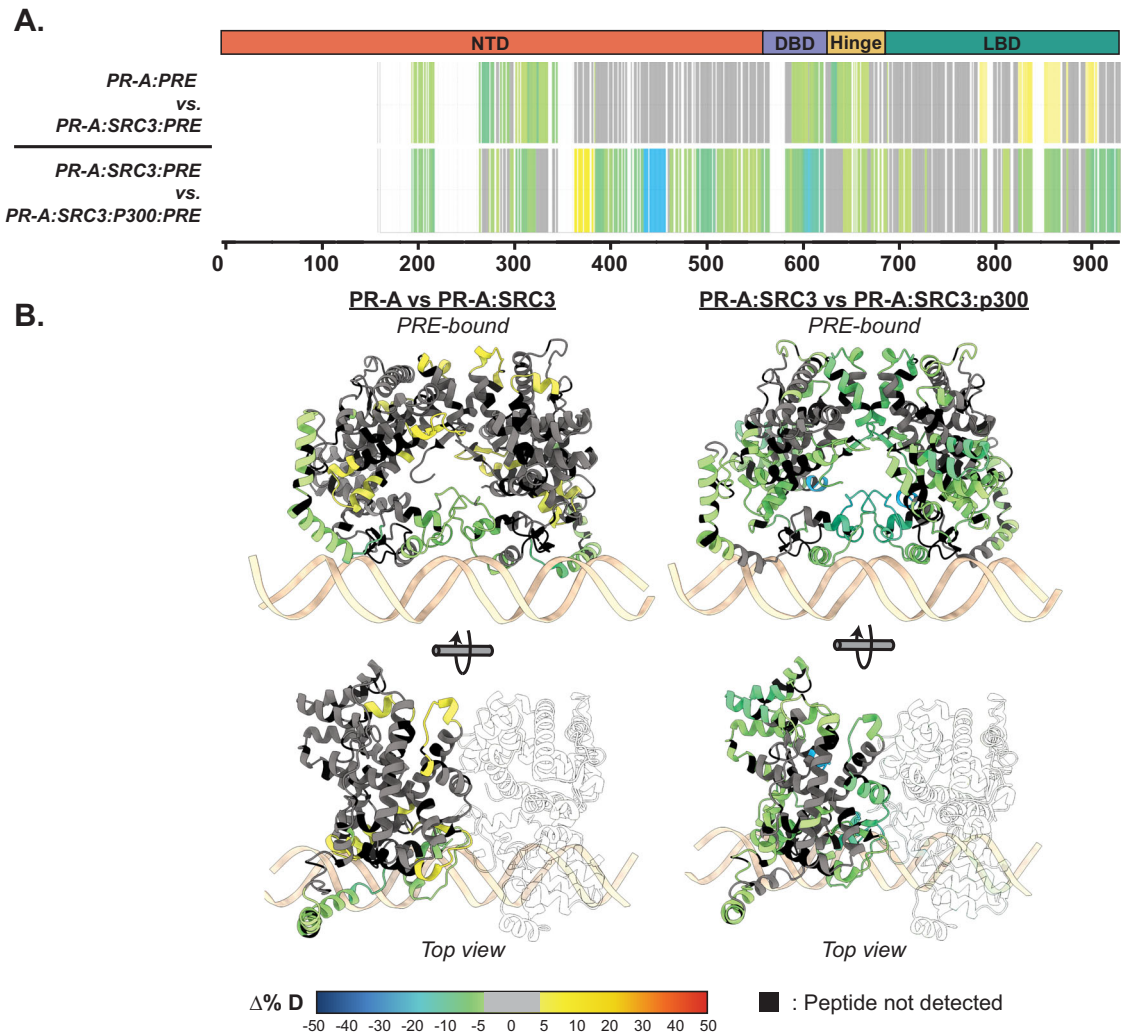

Fig. 4 | p300 differentially alters the conformational dynamics of PR-A and PR-B within the PR:SRC3:p300 complex. A Consolidated HDX plots of PR-A showing the differential HDX-MS comparisons within the plot to the left. Changes in deuterium uptake are represented by the rainbow plot shown, where darker blues correspond to decreased differential deuterium exchange and warmer reds correspond to increases in differential deuterium exchange. Common PR domains are highlighted above consolidated data: N-terminal domain (NTD, orange), DNA-binding domain (DBD, purple), Hinge (yellow), and ligand-binding domain (LBD, teal). **B** AlphaFold3.0 models of PR from the AF1 to LBD (amino acids 456-933 using PR-B numbering). HDX-MS overlays represent the same experiments as the consolidated views in A. Each color represents the percent change in deuterium incorporation (Δ%D), following the scale shown at the bottom. Exchange data is representative of a full seven-timepoint differential HDX experiment with sample injection after 10, 30, 60, 300, 900, and 3600 s of deuterium exchange. Gray overlays indicate no significant changes, and black indicates peptides not detected in the HDX-MS experiment.

through direct PR-p300 interactions or strengthening the PR:SRC3 interaction. This behavior was only measured with PR-A, where we found a concerted shift from deprotected to protected regions in the PRE-containing complexes (Fig. 4). This points to p300-mediated increased complex stability for the PR-A-containing complexes.

Crosslinking results trended similarly, where multiple interactions were found between PR, SRC3, and p300 using combined non-DNA-bound and DNA-bound crosslinking data (Supplementary Fig. 14). These crosslinks between all three proteins point to increased stability of the PR:SRC3:p300 ternary complex, compared to the PR:SRC3 complex (Supplementary Fig. 13). Unlike the HDX-MS data, XL-MS showed no major differences between isoforms. Each PR isoform showed a distinct feature at the C-terminus, where the crosslinking between the three proteins converged. This coincided with the AF2 domain of PR, the acetyltransferase domain of SRC3, and the NCOA2 interaction domain of p300 (p300 amino acids 2041-2240), which could serve as a specific activation point for PR-mediated transcription.

Structural proteomics identifies SRC3 and p300 NR-box utilization for PR isoforms

SRC3 contains conserved domains known as nuclear receptor (NR) boxes. NR-boxes are sequences that mediate binding with AF2 of nuclear receptors through an LXXLL motif. For SRC3, there are three separate NR boxes where PR has the potential to bind (amino acids 685–689, 738–742, and 1057–1061). It is unknown, though, which or how many of these are necessary for the PR:SRC3 interaction. Prior data has identified PR utilization of a combination of NR-box 1 and 2 for SRC1-mediated activation[71–73], yet this has not been established for SRC3. Using HDX-MS, deuterium exchange profiles can be monitored for multiple proteins within a singular experiment. Using the same results for assessing PR-specific exchange, solvent exchange differences were measured for SRC3 to identify PR and p300 binding sites. Differential HDX-MS experiments showed decreased deuterium exchange at NR-box 2 upon PR-A addition and smaller decreases in NR-box 1 (Fig. 5). Interestingly at NR-box 3, increases in solvent exchange were observed, showing greater solvent accessibility in this

https://doi.org/10.1038/s41467-025-59458-y

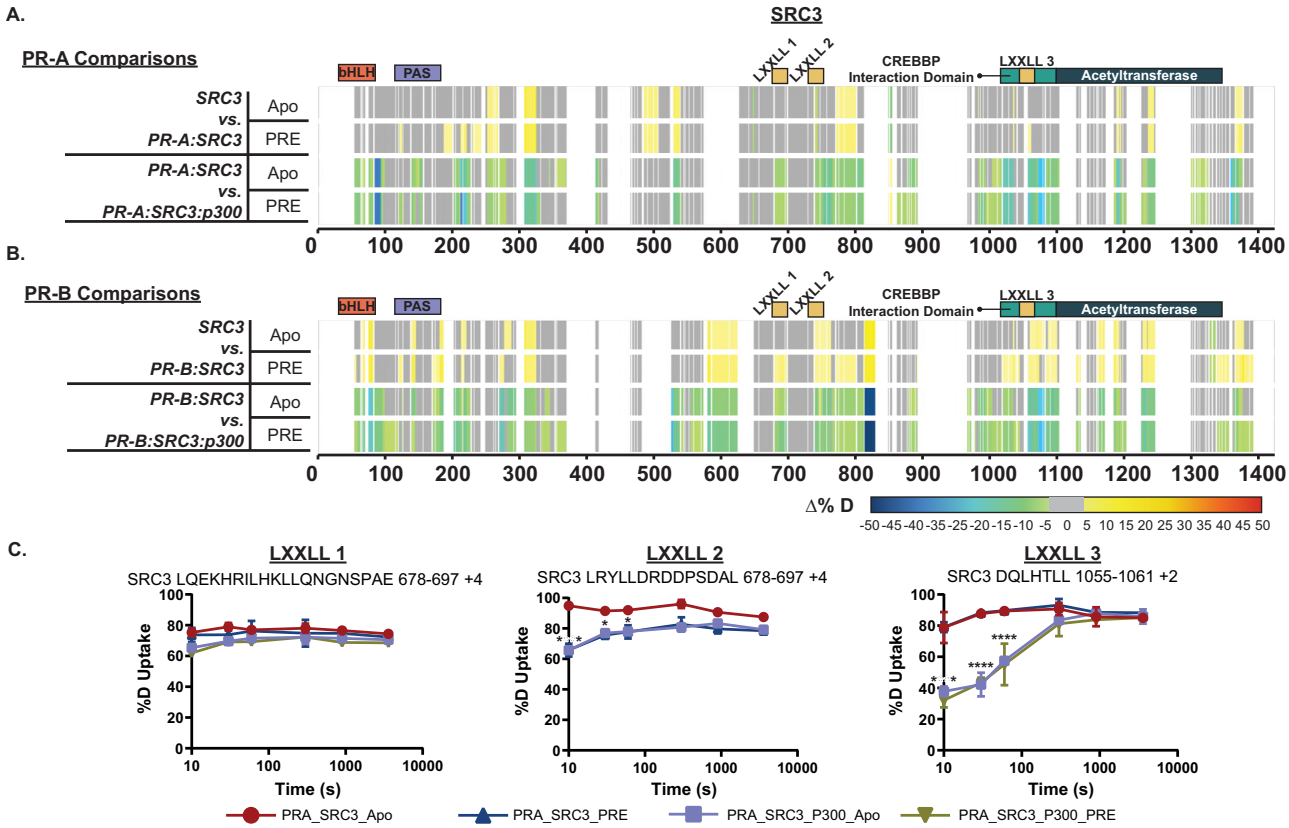

Fig. 5 | PR-A and PR-B differentially interact with SRC3 and are stabilized by p300 addition. A. Consolidated differential HDX-MS results for SRC3, comparing the changes induced by PR-A and p300 binding in the presence and absence of PRE DNA. **B** Consolidated HDX-MS plot of SRC3 exchange, with PR-B comparisons in the same order as PR-A. The motifs highlighted are the following: bHLH (orange), PAS (purple), LXXLL motifs (yellow), CREBBP Interaction Domain (teal), and acetyltransferase domain (dark blue). Each color represents the percent change in deuterium incorporation (Δ%D), following the scale shown, where darker blues correspond to decreased differential deuterium exchange and warmer reds correspond to increases in differential deuterium exchange. Gray overlays indicate no significant changes, and black indicates peptides not detected in the HDX-MS experiment. **C** Selected deuterium uptake plots for peptides that contain LXXLL motifs 1, 2, and 3. The %D uptake indicates the percent deuterium uptake over time for the PR-A:SRC3 ± DNA and PR-A:SRC3:p300 ± DNA HDX experiments. Data points are the mean of three replicates ($N = 3$) with error bars corresponding to the standard deviation in the differential deuterium uptake for each time point. Statistics were derived using two-way ANOVA with Tukey post hoc correction for multiple comparisons, $^{*}p < 0.05$, $^{**}p < 0.01$, $^{***}p < 0.001$, $^{****}p < 0.0001$. Exchange data is representative of a full seven-timepoint differential HDX experiment with sample injection after 10, 30, 60, 300, 900, and 3600 s of deuterium exchange.

region (Fig. 5). These data suggest that NR-box 2 is initially utilized by PR-A, NR-box 1 is utilized to a lesser extent, and the third NR-box remains unbound in both the PR-A apo and PRE-bound state. In addition, we utilized a Bayesian inference method previously validated for HDX-MS experiments[74], which gave us increased confidence in the identity and order of NR-box interactions (Supplementary Fig. 15).

Upon p300 addition, all NR-boxes showed reduced deuterium exchange in both PR:SRC3:p300 and PR:SRC3:p300:PRE differential HDX experiments, including NR-box 3 (Fig. 5). Observing the percent deuterium uptake curves for representative peptides of each NR-box, a nearly two-fold decrease in the deuterium exchange was measured for NR-box 3 upon p300 addition (Fig. 5). Since NR-box 3 was not protected in the absence of p300 in the PR:SRC3 complex, this implies that p300 directly binds NR-box 3. This is further supported by the crosslinking data, where PR formed crosslinks near NR-boxes 1 and 2 of SRC3 and p300 crosslinks with the third NR-box in SRC3 (Supplementary Fig. 14). These crosslinks were the result of combining the crosslinks from non-DNA-bound and DNA-bound complexes, demonstrating that crosslinking was not dependent on PR isoform. There were no significant changes in crosslinks to SRC3 NR-boxes when crosslinks were separated by DNA presence; PR only bound NR-boxes 1 and 2, and p300 only bound NR-box 3. In addition, p300 induced widespread protection throughout PR and SRC3, seen in concerted decreases in deuterium exchange. Taken together, these data indicate that p300 stabilizes both PR and SRC3 in both the absence and presence of DNA.

Similar comparisons were made using PR-B, which showed distinct deuterium exchange compared to PR-A. In the SRC3 ± PR-B experiments, no reductions in solvent exchange were observed in any NR-box. However, solvent exchange increased in NR-boxes 2 and 3 upon PR binding, regardless of PRE presence. Increases in exchange in NR-box 1 were only observed in the presence of PRE. Upon p300 binding, there was deuterium exchange protection in each NR-box, different than the sequential binding seen with PR-A (Fig. 5). The other SRC3 domains, though, have a similar protection pattern to PR-A, where the bHLH, PAS, CREBBP interaction domain, and putative acetyltransferase domains were protected only in the presence of p300, most likely indicating direct p300 binding at those regions. This also supports that PR-A is the primary binding protein of SRC3 instead of PR-B, identified from reductions in solvent exchange upon PR-A – but not PR-B – binding at each NR-box. PR-B, though, still interacted with SRC3. The crosslinking showed that PR-B:SRC3 interactions were within NR-boxes 1 and 2, whereas NR-box 3 only contains crosslinks between SRC3 and p300, the same as PR-A (Supplementary Fig. 14).

Functional mutagenesis corroborates structural proteomics data

To gauge the necessity of each NR-box for PR transcription, promoter-reporter assays were used in conjunction with SRC3 site-directed mutagenesis to measure PR transcriptional output. PR transcriptional response was indirectly measured using a PRE-firefly luciferase reporter plasmid[75]. It has been established that NR-box activity can be ablated through LL to AA point mutants[73,76,77]. Mutating SRC3 NR-box 2 from LXXLL to LXXAA resulted in reduced PR transcriptional response measured through reduced luciferase activity (Supplementary Fig. 16). Changing other NR-box sequences to LXXAA at either Box 1 or Box 3 did not result in reduced PR activity (Supplementary Fig. 16). However, the combination mutant NR-boxes 1 + 3 and 1 + 2 + 3 did reduce PR activity. The SRC3 Box 1 + 2 mutant increased overall activity, which was unexpected considering the HDX data and crosslinking indicated primary interactions at those sites (Supplementary Fig. 16). However, the p160 family of nuclear receptor co-activators, which includes SRC3, has two other members: SRC1 and SRC2, which may be contributing to the maintained PR transcriptional response. In the case where PR can't bind one co-regulator, our data supports that another might be used in its place as a potential compensatory mechanism. The mutation of all three NR-boxes also showed significant differences between WT PR-B and WT-SRC3, though not to the same extent as the other NR-box mutants. This supports the hypothesis that NR-box ablation may lead to alternative co-activator usage. In all, these results show NR-box 2 is an important PR interaction site for transcriptional response, and combination mutants involving NR-box 3 are deleterious to PR activity. These assays were repeated with PR-A, and these responses followed the same trends as PR-B (Supplementary Fig. 16). PR-A transcriptional response fold changes were reduced, consistent with reported reduced transcriptional activity of the A isoform. The SRC3 NR-box 2-3 combination mutant showed a concerted increase in transcriptional activity compared to WT SRC3, which was unexpected. It is possible that the SRC3 NR-box 2-3 mutant may be sufficient to oppose PR-A transcriptional repression. It seems unlikely that PR-A would recruit alternative CoRs due to complete NR-box ablation leading to reduced transcriptional response, consistent with its reported role. Yet, it seems PR-A and PR-B diverge in their responses to these NR-box mutations. Future studies should be conducted to discern the structural consequences of NR-box mutations and build upon what is reported here.

Direct PR:p300 interaction in the absence of SRC3

Previous data had shown that sequential addition of p160 CoRs and p300 influences NR transcriptional response[44,45]. However, the crosslinking results of the PR:SRC3:p300 ternary complex suggested direct PR-p300 binding (Supplementary Fig. 14). Based on these crosslinking results, direct PR-p300 interactions were investigated by XL-MS. In the absence of SRC3, PR and p300 formed crosslinks, indicating direct protein-protein interactions (Fig. 6). Crosslinks to both the N-terminus and C-terminus show that there are multi-pronged PR-p300 interactions without SRC3. These included crosslinks to the p300 NR-boxes, bromodomain, and core acetyltransferase regions.

RU486-antagonism reorganizes PR:SRC3 and PR:SRC3:p300 protein complexes

The logical sequitur for R5020-bound PR led us to investigate the organization of complexes with PR bound to the progestin antagonist, RU486. As determined by SEC-MALS, both PR-A and PR-B bound to RU486 showed monomeric MW distribution in the absence of DNA (Supplementary Fig. 17). With the addition of DNA, both PR isoforms assembled as a DNA complex with an experimentally determined MW within the expected theoretical for PR-A and PR-B dimers (Supplementary Fig. 17 and Supplementary Table 1). This behavior of purified PR bound to RU486 is consistent with previous studies demonstrating RU486 promotes efficient PR dimerization and binding to PRE DNA[3,78,79]. Prior work with PR bound to RU486 showed that the C-terminal tail of the LBD adopts a distinct conformation from that of agonist bound PR[80,81] and X-ray crystallography of PR LBD bound to RU486 results in a displacement of helix 12 in multiple potential conformations that may interfere with formation of an AF2 interaction surface for binding LXXLL motifs of co-activators[41]. X-ray crystallography of the PR LBD bound to antagonists related to RU486 further shows a displacement of helix 12 from the agonist conformation and differential binding of peptides from the corepressors NCoR and SMRT[82]. Studies to date have not explored the influence of RU486 on interactions of PR and CoRs, each as full-length proteins, to explore the potential role of PR interaction surfaces outside of the LBD.

We utilized a similar strategy to the R5020-bound PR experiments to define PR-CoR interactions with PR in an inactive conformation. XL-MS and HDX-MS showed different PR:SRC3 binding modalities than agonist-bound PR. In the agonist-bound complex, PR:SRC3 crosslinks group near the C-terminus of both proteins. However, when RU486-bound, the enriched crosslinks shift from a C-terminal to an N-terminal grouping (Fig. 7A). This suggests that the proteins can still interact, even in an 'inactive' (RU486-bound) state. Interestingly, a marked difference was observed for intraprotein crosslinking. In the presence of RU486, fewer intraprotein crosslinks were observed in PR-B, while more intraprotein crosslinks were observed in SRC3 as compared with agonist (Fig. 7A). These results seem to indicate additional PR-B contacts when bound to agonist, suggesting a PR-B dimerization event.

Conversely, this is not seen in RU486 samples, where RU486-specific PR-B intraprotein crosslinks are reduced. However, a similar

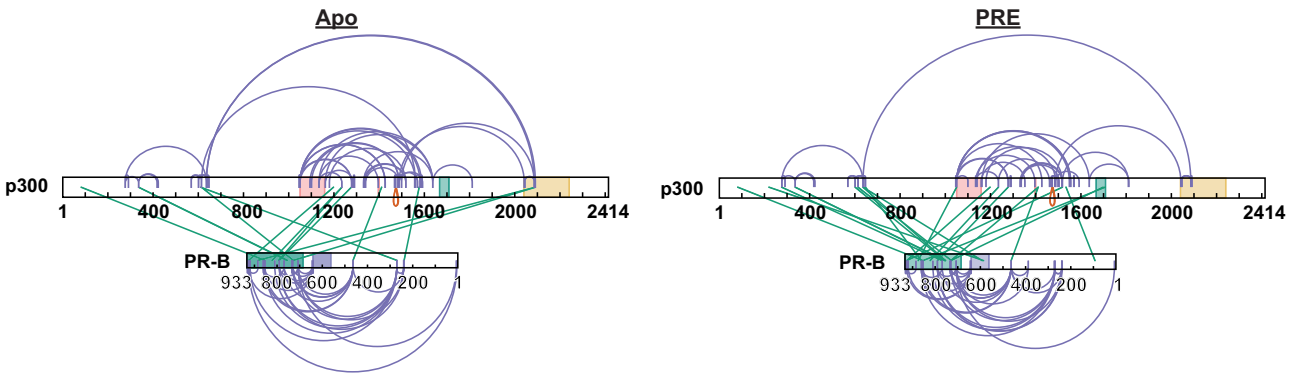

Fig. 6 | XL-MS shows p300 directly interacts with PR. Crosslinking results from PR-B:p300±PRE experiments. Purple: intraprotein crosslinks, green: interprotein crosslinks. PR highlighted domains: DBD (purple) and LBD (green). p300 highlighted domains: bromodomain (pink), zinc finger domain (green), and NCOA2-interaction domain (yellow).

https://doi.org/10.1038/s41467-025-59458-y

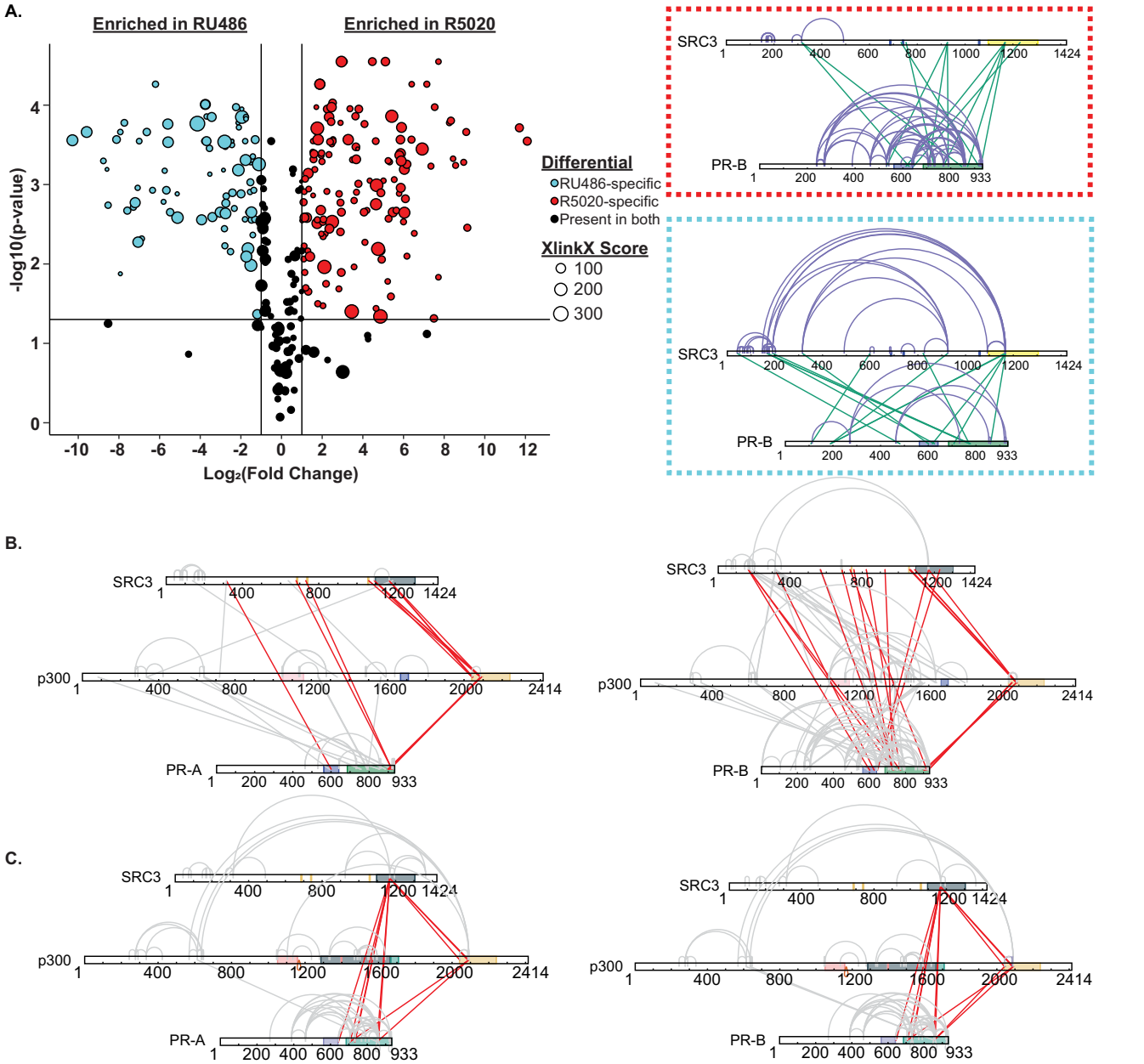

Fig. 7 | RU486 antagonism rearranges PR-SRC3-p300 interactions. A Plotted differential crosslinks in PR-B:SRC3 experiments, comparing R5020-specific (agonist, red) and RU486-specific (antagonist, blue) crosslinks. The *x*-axis represents the Log2 transformed fold change values from Skyline, while the y-axis represents the -log10 transformation of the Skyline p-value output. The lines are indicative of a Log2 fold change of 1 (two-fold increase) and -log10 *p*-value of 1.3, corresponding to $p < 0.05$. Each point represents a unique crosslink with corresponding XlinkX scores represented as point size. *P*-values were calculated by pairwise-ratio comparisons of the transition peak areas for crosslinked peptides in Skyline using linear mixed-effects models within the MSStats group comparison node[115]. **A Red**. XlinkX view of R5020-specific crosslinks in differential PR:SRC3 experiments. **A Blue**. XlinkX view of RU486-specific crosslinks in differential PR:SRC3 experiments. **B** All validated R5020-bound crosslinks for differential PR-A:SRC3:p300 ± PRE (Left) and PR-B:SRC3:p300 ± PRE (Right) experiments. Selected crosslinks, highlighted in red, show PR: SRC3-specific crosslinks. **C** All validated RU486-specific crosslinks for the same experimental setup described in B. Red denotes all PR:SRC3 crosslinks detected with an XlinkX score ≥ 50. Defined domains are as follows: PR - DBD (purple) and LBD (green); SRC3 – NR-boxes (gold) and histone acetyltransferase domain (violet); p300 - bromodomain (pink), zinc finger domain (green), and NCOA2-interaction domain (yellow).

number of interprotein crosslinks remain, implying that this complex is loosely formed but held together by SRC3. Further crosslinking in the PR:SRC3:p300 ternary complex showed crosslinks between PR, SRC3, and p300, suggesting all three proteins can interact when antagonist bound. The most apparent difference for the RU486 crosslinking was the concerted loss of crosslinking between PR and p300 at the NR-boxes (Fig. 7C). This may be indicative of a transition from an active to inactive state for PR:SRC3:p300 driven transcription. This inactive state makes sense, since the C-terminal AF2 should still be in proximity to the CoRs but is not positioned in a way that is conducive to transcriptional activation. In this, SRC3 could act as a molecular switch for PR-mediated transcription, where binding to the NR-boxes is required for transcriptional response. Moreover, the crosslinks between p300 and NR-box 3 within SRC3 were lost upon RU486 binding of the receptor (Fig. 7C). This supports that PR, in its inactive state, can still form contacts with SRC3 and p300 at their

https://doi.org/10.1038/s41467-025-59458-y

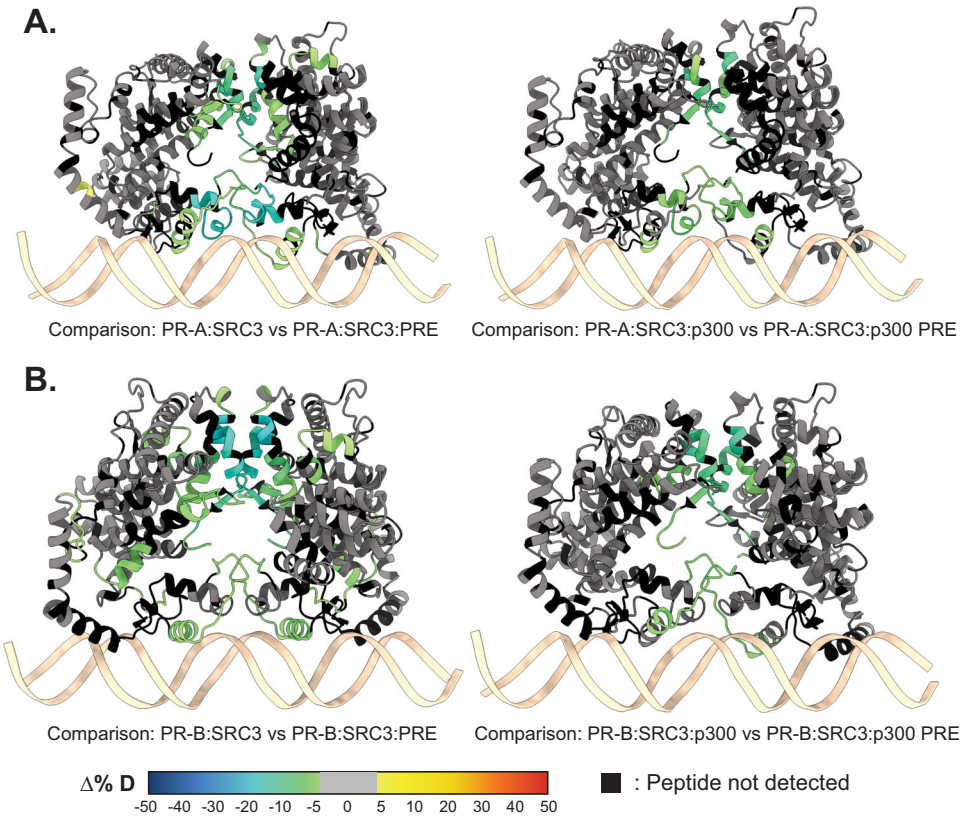

Fig. 8 | RU486-bound PR has reduced deuterium exchange upon CoR binding. **A** PR models of AF1 to C-terminus (amino acids 456-933) with PR-A HDX overlays, corresponding to the comparisons shown beneath them. **B** PR models of the AF1 to C-terminus with corresponding PR-B HDX overlays labeled beneath. Each color represents the percent change in deuterium incorporation (Δ%D), following the scale shown at the bottom. Gray overlays indicate no significant changes, and black indicates peptides not detected in the HDX-MS experiment. Exchange data is representative of a full seven-timepoint differential HDX experiment with sample injection after 10, 30, 60, 300, 900, and 3600 s of deuterium exchange.

respective C-termini. Comparing the ternary complex to the PR:SRC3 complex in Fig. 7A, we see there are differences in the total number of inter and intraprotein crosslinks. This was due in part to using a score cut-off for high-confidence visualization purposes; however, the interprotein crosslinks do not completely disappear, but rather rearrange. The reduced number of crosslinks may also indicate the reduced affinity these proteins have for one another when PR is antagonist-bound; however, XL-MS supports complex formation and p300 induction of complex stability, which does not seem to be ligand-specific. These XL-MS results challenge the classical NR model, where antagonist-bound protein cannot interact with coactivators.

To validate whether these complexes were formed in the presence of RU486, HDX-MS was used to investigate the backbone dynamics of each protein while RU486-bound and in complex. Distinctive from the R5020-bound complexes, the presence of an antagonist significantly reduced deuterium exchange, specifically in all the PR ± PRE experiments, leading to reduced deuterium exchange throughout the protein (Supplementary Fig. 18). However, the sequential addition of co-regulators showed an expected solvent exchange profile, by comparison. Because of this, comparisons were made exclusively between the larger ternary complexes. Interestingly, regions of decreased deuterium exchange were observed for the larger ternary complexes with both PR-A and PR-B for ± DNA experiments (Fig. 8). The differential deuterium uptake was similar to that seen with agonist (R5020)-bound PR in Fig. 3. Protected regions were localized to the DBD, CTE, and LBD, all regions known to interact with DNA and CoRs. In addition, portions of the AF1 and AF2 cleft had reduced deuterium exchange (Fig. 8), which is a hallmark of CoR binding. The most notable result was that CoR addition resulted in a stronger stabilization of both PR dimerization domains. This suggests that when antagonist-bound, PR can still associate with co-activators: SRC3 and p300, and these CoRs still help to stabilize PR in a complex.

Discussion

Steroid hormone receptors (SR) are hormone-responsive transcription factors that exhibit remarkable functional diversity in mediating cell and target gene-specific responses. These responses are largely driven by conformational dynamics of the receptor, enabling their binding of distinct subsets of transcriptional CoRs and DNA response elements. Because of their presence in various cancer phenotypes, SRs are attractive targets for cancer therapeutics through the disruption of their transcriptional activity. Because of the challenges and limitations of traditional macromolecular structure approaches for analysis of large conformationally dynamic proteins, XL-MS and HDX-MS were used here to make solution-phase structural measurements of amino acid distance constraints between protein components and to probe conformational dynamics of PR-A and PR-B in complex with SRC3, p300, and PRE DNA. This approach was made possible by two advancements. One was the ability to generate high-quality purified full-length PR and CoRs and assemble stable complexes under native conditions, and the other was technical developments by improving MS protein coverage for structural proteomics studies. The current studies focused on the analysis of each PR isoform separately. PR-A and PR-B are capable of forming heterodimers, as shown previously in vivo by traditional two-hybrid assay, and in vitro by gel electrophoretic mobility shift assay (EMSA) when complexed with PRE DNA[79]. However, mixing isoforms generates approximately equal ratio mixtures of PR-A and PR-B homodimers and PR-A/PR-B heterodimers since

dimerization interfaces are in equilibrium. Because of the complex challenge of isolating a pure population of PR-A/PR-B heterodimers, we focused the present studies on individual PR isoforms. As discussed in the Introduction, this analysis is biologically relevant since one or the other PR isoforms are expressed predominantly, and are more functionally important, in several target tissues and cell types under normal conditions, and in some endocrine tumors and disorders.

As expected, our results show both PR-A and PR-B binding to DNA as dimer. It had been hypothesized that DNA binding induces compact structure, particularly in the ID NTD and other structurally flexible regions. The differential XL-MS data showed DNA-mediated changes to PR organization. Crosslinks enriched in DNA-bound PR indicated that DNA induces LBD movement away from the NTD, suggesting that PR converts from a compact to an elongated structure upon DNA binding. These are interesting findings and provide much-needed information regarding the structural dynamics of PR that would likely apply to other members of the SR sub-family. Several studies show that PR-A and PR-B are functionally unique transcriptional regulators, capable of differentially regulating gene transcription depending on isoform and promoter[15,28,83–85]. Therefore, it is possible that structural dynamics with the PR-A and PR-B upon PRE binding may be dependent on specific promoters within the whole genome, and thereby providing the flexibility for inclusion or exclusion of the set of CoR complexes under in vivo conditions. Other studies suggest that each isoform adopts distinct conformations within the cell, allowing PR-A to interact with a set of CoRs that are different from those which interact with PR-B[86–88]. Our differential HDX for each isoform with CoRs and response element DNA supports the possibility of varying affinities for CoRs depending on PR isoform. Our findings are further supported by previous studies showing that PR binding to multiple PREs occurs in a cooperative fashion and PR-B has a greater cooperative binding ability than PR-A suggesting that conformational dynamics of each PR isoform and the chromatin conformation of the regulatory regions of the target gene are fundamental for their specific activity[89,90].

The HDX-MS experiments were imperative for us to understand the role each CoR plays in PR transcriptional complex formation. Reduced deuterium exchange observed throughout PR-A following the binding of SRC-3, particularly in the PR dimerization region, suggested that that SRC3 may induce PR-A dimerization without the addition of PRE DNA. This could be an activation step unique to PR-A where hormone release from heat shock proteins/immunophilins prior to binding genomic PRE DNA is stabilized by interactions with SRC3. This is further supported by several structural studies that show a series of protein binding events that serve to activate steroid receptors in the cytoplasm[91,92]. It is plausible that SRC3 may serve as a stabilizing binding protein for PR that is primarily localized in the nucleus as compared with PR-B that is localized between the nucleus and cytoplasm, and undergoes a shift to complete nuclear localization upon hormone activation[38,39]. When DNA bound, we observed increases in deuterium incorporation for PR-A that were unexpected, but these increases were not in the dimerization or AF2 domains. Based on these observations, it can be hypothesized that such conformational changes may be important in preparing PR-A surfaces for interactions with other CoRs and to facilitate the process of the exclusion or inclusion of specific CoRs in the complex. This is a phenomenon commonly adopted by SRs, where distinct CoRs bind SRs when moving from one DNA site to another one in the genome[93–95]. However, the differential deuterium exchange was not as pronounced in PR-B, suggesting PR-A is the primary interacting isoform in the PR:SRC3 ternary complex. This differs from prior work showing SRC1 and SRC2 preference for PR-B in other cell types[44,73,96–98]. SRC3 is known to be an oncogenic CoR in breast cancer. The preference of SRC3 to bind PR-A could contribute to the worse outcomes of breast cancers that overexpress excess PR-A, considering SRC3 is an independent cancer driver currently being targeted for therapeutics[99]. Evidence suggests that PR-A and PR-B may have different affinities for a common set of CoRs as well as the ability to recruit different co-factors, suggesting that tissue distribution and expression of CoRs is also a likely determinant of diverse activities of PR isoforms[21,98,100].

The perturbations in differential PR HDX, induced by SRC3 and p300, showed that these CoRs act in a mutually beneficial fashion. This was evidenced by the initial regions of increased deuterium exchange within PR when SRC3 was bound, which became protected from deuterium exchange once p300 was added. Using this sequential addition strategy, we assessed the contribution of each CoR on PR deuterium exchange to show that SRC3 prepares PR for additional CoR binding while p300 stabilizes the ternary complex. Aside from the PR changes, we identified NR-boxes 1 and 2 as being the main PR interaction sites on SRC3, while p300 exclusively used NR-box 3, confirmed by both HDX and XL-MS. These findings indicate a probable transcriptional activation mechanism in PR:SRC3:p300-driven transcription, where NR box occupancy serves as a transcriptional activator. The C-terminal portions of each ternary complex member remained in proximity, likely resulting in enhanced acetyltransferase activity by SRC3 and p300. This would be in agreement with available cryo-EM structures with PR-B in complex with SRC2, placing the PR carboxy-terminus in proximity to p300 for direct binding and further recruitment of transcription factors[43]. Yet, our data demonstrates that this is true for PR-A as well, indicating that these isoforms interact very similarly but remain context-dependent.

One insight provided by our MS proteomics approach is that PR liganded with the antagonist RU486 retained interactions with SRC3 and p300, but exhibiting different interactions than PR bound to agonist (Figs. 7, 8). Previous studies showing impaired binding of coactivators in exchange for increased binding by co-repressors were restricted to the analysis of CoR peptide interactions with the LBD-AF2 region of PR liganded with the antagonist. The study here examined interactions with full-length PR and CoRs. In the presence of RU486, our analysis indicated major changes in intraprotein crosslinks in both PR and SRC3, a shift in interprotein interaction surfaces from C-terminal to N-terminal regions of both PR and SRC3, and a loss of interaction between PR and NR boxes, but not other regions of p300. This challenges our understanding of the mechanism of repression of nuclear receptor activity by antagonists that may not be as simplistic as previously thought. Our results support the conclusion that interaction surfaces between the same CoRs change between an active and repressed PR complex. Whether these changes represent different binding affinities is not known, nor is it known whether other CoRs, including corepressors, can also bind either simultaneously or preferentially in place of SRC3 and p300. A difference in binding affinity could prefer one transcriptional complex composition over the other. Our data suggests possible mechanisms for a repressive PR:SRC3:p300 antagonist-bound complex through positional orientation of the HAT domain of p300 that is no longer in proximity to histones to mediate acetylation required for transcriptional read through. In addition, the loss of PR binding with NR-boxes of p300 could also contribute to suppressed transcriptional activity. Interestingly, partial agonist activity of RU486 is mediated only by PR-B in response to activation of cellular protein phosphorylation signaling pathways and phosphorylation in the NTD; however, differences in co-activator recruitment do not appear to be involved[101]. However, as shown we find that both isoforms are capable of interactions with co-activators SRC3 and p300. PR-A and PR-B are also reported to respond differently to RU486, whose antagonist, or even PR-B specific agonist activity in specific cell contexts is dependent on NTD conformation and its post-translational modification[101,102].

Structural proteomics, through HDX and XL-MS, combined with AlphaFold 3.0-driven structure predictions, provided insights into structures and conformational dynamics of PR:CoR:DNA complexes. Our results indicated that PR:SRC3 complexes have distinct structures

depending on their DNA occupancy. We uncovered a sequential priming mechanism for PR, whereby it binds DNA, then SRC3 to stabilize the dimer, and lastly p300 to stabilize the ternary complex. These details showed that p300 interacts not only with the PR C-terminus but the PR N-terminus as well, likely to position its HAT domain near DNA and chromatin. In addition, NR box preference indicates a specific order of complex assembly. Loss of NR-box site interactions in the presence of the antagonist RU486 results in a reduction in PR transcriptional response, highlighting their necessity in PR:SRC3:p300-mediated transcriptional activity. Contrary to prior understanding, SRC3 and p300 remain associated with PR when bound to antagonist, although the orientation of the complex differs from that observed with an agonist, suggesting antagonist-driven rearrangement of the transcriptional complex. We show that co-activators SRC3 and p300 stabilize the PR dimer when it is in an 'inactive' conformation liganded with RU486, implying these interactions are affinity-driven and context-dependent. Collectively, the findings presented here elucidate how SRC3 and p300 interact at the amino-acid level with PR-A and PR-B, influencing their conformation and activity.

Methods

Materials

Oligonucleotides (Sigma-Aldrich). 32-mer progesterone response element (PRE) dsDNA sequences: Sense: 5′-CATCTTTGAGAACAAACTG TTCTTAAAACGAG-3′; Antisense: 5′-CTCGTTTTAAGAACAGTTTG TTCTCAAAGATG-3′. Sigma-Aldrich provided Disodium hydrogen phosphate (Na_2HPO_4) (S9763), Sodium Chloride (NaCl) (S9888), Urea (51456), Benzonase (9025-65-4), and 2-Mercaptoethanol (2ME) (M3148). Fisher Scientific provided Glycerol (BP229-4) and Biotin (B0463). Hampton Research provided TCEP Hydrochloride (50-093-0). Invitrogen provided UltraPure™ 0.5 M EDTA (15575020) and SYPRO Gel filtration standard (S6650). BIO-RAD provided an unstained protein standard (1610363) and Gel Filtration Standard (1511901). Thermo Fisher provided Zeba™ Spin Desalting Columns 7 K MWCO 0.5 mL (89882) and Disposable PES Bottle 0.2uM Top Filters (166-0045).

Plasmids

Progesterone receptor protein-expression plasmids: pRP[Exp]- EGFP/PuroEF1A>hRluc(ns):P2A:hPGR[NM_000926.4] (co)* and pRP[Exp]-EGFP/PuroEF1A>hRluc(ns):P2A:hPGR[NM_001202474.3] (co)*, were constructed using VectorBuilder. Their respective vector IDs are VB230919-1497uvg and VB230919-1498ukn, which can be used to retrieve detailed information about the vector at vectorbuilder.com. Progesterone response plasmid, 4X PRE TK luc, was a gift from Renee van Amerongen[75] (Addgene plasmid # 206159; http://n2t.net/addgene:206159; RRID:Addgene_206159). Lentiviral vectors were constructed to stably express the 4xPRE response vector upstream of a firefly luciferase, using a minimal promoter. This vector was based on another from the van Amerongen lab using a minimal YB-TATA promoter[75]. This vector was constructed using VectorBuilder, under the vector ID VB240826-1684qpq representing pLV[Exp]-mCherry:T2A:Hygro-4xPRE-2YBTATA > Luc2. SRC3 mutants were made from the human NCOA3 transcript (NCBI, NP_858045.1) in the pSport6 expression vector.

Site-directed mutagenesis

Point mutants were designed with the Takara Bio online primer design tool. Primers were generated for the LXXLL to LXXAA mutants for each NR-box, and mutagenic PCR was performed using the PrimeStar DNA Max polymerase with subsequent In-Fusion assembly. Mutants were validated using whole plasmid sequencing (Genewiz), assessing the confidence of the mutated region. Co-mutations (e.g., NR-box 1 and 2) were performed by mutating one site, validating, then mutating the other site with subsequent validations. Mutagenic primers were purchased from Sigma-Aldrich and the sequences are as follows: SRC3 NR-box 1 (Forward 5′-*ACAAGGCGGCGCAGAATGGGAATTCACCAGC*-3′ Reverse 5′-*TCTGCGCCGCCTTGTGCAAAATCCGGTGC-3*′); SRC3 NR-box 2 (Forward 5′-*GATACGCGGCGGACAGGGATGATCCTAGTGATG*-3′ Reverse 5′-*TGTCCGCCGCGTATCTAAGAAGTGCATTATTCTCC*-3′); SRC3 NR-box 3 (Forward 5′-*ACACTGCTGCCAGCAACACAGATGCCACAGG*-3′ Reverse 5′-*TGCTGGCAGCAGTGTGCAGCTGGTCCAATAATG*-3′).

Stable cell line generation

Lentiviral 4xPRE-2YBTATA (VB240826-1684qpq, VectorBuilder) was packaged by VectorBuilder prior to stable cell line generation. Packaged vector was added to 293 T cells at a concentration of 1E + 06 TU/mL, supplemented with 10 µg/mL polybrene. Cells were incubated overnight in a humidified 5% CO_2 incubator. Polybrene and virus was aspirated, and the cell media was replaced with fresh DMEM supplemented with 10% FBS and 250 µg/mL Hygromycin B (ThermoFisher 10687010) for 1 week. Cells were maintained in Hygromycin-containing media and passaged twice. Stably expressing cells were sorted into 96-well plates as single cells by fluorescence-activated cell sorting using the mCherry channel. Clones were selected and tested against non-infected controls to confirm transcriptional response.

Progesterone receptor response assays

PR protein expression and response assays were co-transfected in 293 T cells (ATCC, CRL-3216) at a 2:1 (protein:response plasmid) ratio using X-TremeGeneHP (Roche, XTGHP-RO) at a 4:1 (X-TremeGene:Plasmid Mix) ratio. Cells were incubated overnight, then re-seeded in 384-well plates (10 µL of 1E + 06 cells/mL suspension) in quadruplicate per transfected sample. Transfected cells were incubated for 4 h at 37 °C in a humidified 5% CO_2 incubator. After 4 h incubation, either vehicle (EtOH), R5020 (Revvity, NLP004005MG), or RU486 (Sigma, M8046) were added at 2x concentration to the transfected cells for a final concentration of 50 nM and final volume of 20 µL. Cells were incubated overnight with the compound, then treated with Dual-Glo® reagents (Promega) by adding an equal volume (20 µL) of firefly luciferase reagent as cell culture volume, incubating for 10 min, then reading on a plate reader. Following firefly luciferase measurements, Stop-Glo Renilla luciferase reagent was added using the same volume as the firefly reagent (20 µL), incubated at room temperature for 10 min, then read on a plate reader, as described on the Promega website[103]. Plates were read on a Bio-Tek Neo II plate reader using a gain of 200 and an integration time of 100 ms. Visualizations were made using GraphPad Prism (GraphPad, v10.4.1). Two-way ANOVA was used with Dunnett's correction for statistical significance.

Protein expression

Human PR-A, PR-B, SRC3, and p300 as full-length open reading frame DNA were each synthesized with optimal codon usage for insect cells with an in-frame Strep II tag (WSHPQFEK/G) and a glycine spacer at the amino-terminus and inserted into pFastBac1 transfer vectors (Epoch Life Sciences, Houston, TX). Recombinant bacmids were generated and expanded in *Spodoptera frugiperda* (*Sf9*) cell cultures and viral titers were determined by plaque assays as previously described[58,59] with the following modifications: multiple 500 mL cultures of *Sf9* cells were infected with recombinant virus at an MOI of 2.0 and incubated for 48 hour at 27 °C in oxygenated spinner vessels. For cells expressing PR-A or PR-B, the progestin agonist R5020 or antagonist RU486 was added to *Sf9* cell cultures at 250 nM for 24 h post-infection. Cells were collected and centrifuged 1500 × *g* for 10 min, and pellets were washed once PBS by resuspension and centrifugation. Cell pellets were flash frozen and stored at −80 °C.

Protein purification

Cell pellets (from 2 × 500 ml cultures) were resuspended in 50 mL of lysis buffer (50 mM Na_2HPO_4, pH 8.0, 500 mM NaCl, 5% Glycerol, 1 M

Urea, 1 mM EDTA, 1 mM βME), supplemented with protease inhibitor tablets (leupeptin, aprotinin, bacitracin, and PMSF) and submitted to Teflon-glass homogenization for 8 strokes at 1.5 speed in the cold room (4 °C). The homogenate was treated with 1.2 units/mL of benzonase nuclease or 1 hour at 4 °C, then passed 3 times through an 18 G needle followed by a 25 G needle. The lysate was centrifuged twice for 1 hour at 50,000 × *g* and the resulting supernatant was filtered using 0.2 µm disposable filters. Purification was performed on AKTA Pure™ 25 at 4 °C while monitoring conductivity and UV. A 1 mL StrepTrap XT prepacked Hi-Trap chromatography column (Cytiva) was equilibrated with lysis buffer for 10 column volumes (CV), and after loading the cleared cell lysate, the column was washed for 30 CV with equilibration buffer and then eluted with equilibration buffer containing 40 mM biotin. Eluted fractions (1 mL) were collected and analyzed by Coomassie Blue-stained 4–15% gradient SDS-PAGE gels. Fractions containing proteins of interest were pooled and concentrated to 1-2 mL by an Amicon ultracentrifugal device with a 10,000 MW cutoff (A280 < 4.0). Proteins were further purified by a preparative size exclusion chromatography (SEC) column (HiLoad 16/600 Superdex 200 pg), degassed and equilibrated in SEC buffer (20 mM Hepes, pH 7.5, 200 mM NaCl, 5% Glycerol, 1 M Urea, and 1 mM TCEP). Elution fractions (1 mL) were collected and analyzed by Coomassie Blue-stained 4-15% gradient SDS-PAGE gels, and peak fractions were concentrated as above. Concentrations of purified protein products were by determined by Nanodrop absorbance at 280/260 nm, calculation of extinction coefficient, and by comparison of purified bands on Coomassie Blue-stained 4–15% SDS-PAGE gel with a standard curve of know amounts of unstained protein markers. Aliquots (50-100 µL) of purified protein were snap frozen in liquid nitrogen and stored at −80 °C for up to 3-4 months, and samples were used only once after thawing.

Analytical SEC

All procedures were conducted at a temperature range of 0 °C to 4 °C. Protein samples (50 µL each) were injected using a capillary syringe into a 50 µL loop and fractionated over a Superdex 6 Increase 5/150 GL column. The column was equilibrated with degassed SEC Buffer (20 mM Hepes, pH 7.5, 200 mM NaCl, 5% Glycerol, 1 M Urea, and 1 mM TCEP) as well as degassed SEC buffer without Urea (20 mM Hepes, pH 7.5, 200 mM NaCl, 5% Glycerol, and 1 mM TCEP). Columns were calibrated using Gel Filtration Standards.

Microfluidic modulation spectroscopy (MMS)

The assessment of the secondary structures of our purified proteins was conducted via Microfluidic Modulation Spectroscopy (MMS) using a fully automated Aurora TX RedShift Biosystem (RedShiftBio, Boxborough, MA, USA). Prior to MMS spectroscopy, proteins were dialyzed overnight in SEC Buffer (20 mM Hepes, pH 7.5, 200 mM NaCl, 5% Glycerol, 1 M Urea, and 1 mM TCEP) to ensure buffer matching. Each protein was measured at a concentration of ~ 1.0 mg/mL. Samples and matching buffer were channeled through a high precision microfluidic flow cell and under continuous flow with 7–30 psi backing pressure and 1 Hz modulation. A mid-infrared quantum cascade laser was used to generate the incident beam, and absorbance was measured by a cadmium detector. Absorbance across the amide I band were collected from wavenumbers 1700–1568 cm^{-1}. The buffer signal was subtracted from the sample signal and then averaged to generate differential absorbance spectra.

Differential absorbance spectra were processed using *delta* analytics software[67]. Spectra were analyzed with a 0.6 nominal displacement factor and fit over a custom range of 1688 to 1620 cm^{-1} to a lysozyme model. Protein concentration fit and protein displacement factor were set to 30% and 20%, respectively. Savitsky-Golay smoothing[104] was applied to second derivative plots generated for all samples with a 19-wavenumber window. Both ends of the second derivative spectra were baselined. The inversion of the baseline-corrected second derivative spectra was then fitted to Gaussian curves. The area of Gaussian curves were used to estimate percentages of higher order structures (HOS).

Size exclusion chromatography-multi-angle light scattering (SEC-MALS)

Data were collected using a Dawn Ambient light scattering instrument equipped with a 661 nm laser (Wyatt). The whole system is linked to an HPLC system with UV absorbance detection at 280 nm (Agilent) and an Optilab (Wyatt) for differential refractive index (dRI) measurements. Approximately 20 to 100 µg of proteins (p300, SRC3, PR-A (agonist R5020 or antagonist RU486), PR-B (R5020 or RU486), or DNA alone or in complexes were injected and flowed through a Superose 6 increase column (Cytiva). Data was analyzed using the Astra software (Wyatt). The BSA sample was also run as a calibration control and to obtain the dn/dc values in the different buffer conditions. The buffer was 20 mM Hepes, 50 mM NaCl, 5% glycerol, 1 mM TCEP, with or without 1 M Urea, pH 7.5. Figures were plotted using the Origin software. Standard errors shown were 5% of the calculated MW.

Mass spectrometry sequencing of purified proteins

The purified protein band from SDS-PAGE gels was excised and processed for in-gel digestion using trypsin enzyme (Pierce 90058). The peptide samples were subjected to nanoflow liquid chromatography tandem mass spectrometry (LC-MS/MS) analysis using nanoLC1000 system coupled to Orbitrap Fusion mass spectrometer (Thermo Scientific, San Jose, CA). Peptide separation was done on a homemade 20 cm × 75 µmI.D. column (Reprosil-Pur Basic C18, 1.9 µm, Dr.Maisch GmbH, Germany) at a flow rate of 200 nL/minute for a 90 min run time. The data was acquired in data-dependent mode for 3 s cycle time. The raw file from MS was searched using Proteome Discoverer (v1.4, Thermo Fisher Scientific, San Jose, CA) with Mascot 2.4 (Matrix Science) against the purified protein sequence of interest, including the termini tags. For SII-PR-B samples, we also included the *Spodoptera frugiperda* protein database (NCBI refseq, updated 2023_11_22) as an insect cell background. The precursor mass tolerance was confined within 20 ppm with fragment mass tolerance of 0.5 dalton and a maximum of two missed cleavages with trypsin/P was allowed. The peptides identified from mascot result file were validated with 5% false discover rate (FDR). The protein sequence coverage map and peptide areas were extracted from the PD1.4 software.

Hydrogen-deuterium exchange mass spectrometry

Peptide identification. Peptides were identified using MS/MS experiments performed on a QExactive (ThermoFisher Scientific, San Jose, CA) over a 70-min gradient. Product ion spectra were acquired in data-dependent mode, and the five most abundant ions were selected for the product ion analysis per scan event. For peptide identification, the MS/MS *.raw data files were analyzed on Sequest (version 2.3, Matrix Science, London, UK). Mass tolerances were set to ± 0.6 Da for precursor ions and ± 10 ppm for fragment ions. Oxidation to methionine was selected for variable modification. Non-specific digestion was selected in the search parameters with 4 missed cleavages. Only peptides with an FDR < 1% were used in the dataset, and duplicate charge states were used for each peptide in the peptide set.

Continuous labeling. Experiments were carried out on a fully automated system (CTC HTS PAL, LEAP Technologies, Carrboro, NC; housed inside a 4 °C cabinet) as previously described[48] with the following modifications: For differential HDX, protein-protein complexes were generated by sequential protein addition, where each protein would incubate for 15 min at 4 °C before sequential addition of the next protein. For larger complexes, the order was as follows: DNA, PR, SRC3, then p300, waiting 15 minutes between each addition. The final incubation was carried out in the sample plate for 30 minutes before the

experiment started (1 h total incubation time from final protein addition). The reactions (5 µL) were mixed with 20 µL of deuterated (D2O-containing) buffer [20 mM Hepes, 200 mM NaCl, 1 M Urea, 1 mM TCEP, and 5% glycerol (pD 7.9)] and incubated at 4 °C for 10, 30, 60, 300, 900, or 3600 s. A non-deuterated control was included for baseline measurements ($t = 0$ s). Following on-exchange, unwanted forward- or back-exchange was minimized, and the protein complex deuteration was stopped by the addition of 25 µL of a quench solution [20 mM NaH_2PO_4 and 1% TFA (pH 2.5)] before immediate online digestion and data acquisition. See also: Supplementary Table 2.

HDX-MS analysis. Samples were digested through an immobilized fungal XIII/pepsin column (1-to-1 ratio, prepared in-house) at 50 µL/min [0.1% (v/v) TFA at 4 °C]. The resulting peptides were trapped and desalted on a 2 mm-by-10 mm C8 trap column (Hypersil Gold, ThermoFisher Scientific). The bound peptides were then gradient-eluted [4 to 40% (v/v) CH_3CN and 0.3% (v/v) formic acid] on a 2.1 mm-by-50 mm C18 separation column (Hypersil Gold, ThermoFisher Scientific) for 5 min. Sample handling and peptide separation were conducted at 4 °C. The eluted peptides were then ionized directly using electrospray ionization, coupled to a high-resolution Orbitrap mass spectrometer (QExactive, ThermoFisher Scientific).

Data rendering. The intensity-weighted mean m/z centroid value of each peptide envelope was calculated and converted into a percentage of deuterium incorporation. This is calculated by determining the observed averages of the undeuterated ($t = 0$ s) and fully deuterated spectra using the conventional formula $D_0 = \frac{<m> - <m_{0\%}>}{<m_{100\%}> - <m_{0\%}>} \cdot N$, where D_0 is the average number of peptide amide deuterons in the protein after incubation for time t, and $<m>$, $<m_{0\%}>$, and $<m_{100\%}>$ are the isotope-averaged centroids of the molecular ion peaks, with N being the total number of peptide amide hydrogens in the peptide, described by Zhongqi Zhang and David L. Smith here[46]. The fully deuterated control, 100% deuterium incorporation, was calculated theoretically, and corrections for back-exchange were estimated to be 70% deuterium recovery, accounting for 80% final deuterium concentration in the sample (1:5 dilution in deuterated buffer). Statistical significance for the differential HDX data is determined by an unpaired t-test for each time point, a procedure that is integrated into the HDX Workbench software[105].

The HDX data from all overlapping peptides were consolidated to individual amino acid values using a residue averaging approach. For each residue, the deuterium incorporation values and peptide lengths from all overlapping peptides were assembled. A weighting function weights shorter peptides more than longer peptides. Weighted deuterium incorporation values were then averaged to produce a single value for each amino acid. The initial two residues of each peptide, as well as prolines, were omitted from the calculations. This approach is similar to other reported methods[106].

Deuterium uptake for each peptide is calculated as the average of %D for all on-exchange time points, and the difference in average %D values between the unbound and bound samples is presented as a heatmap with a color code given at the bottom of each figure (warm colors for increased deuterium exchange [deprotection] and cool colors for decreased deuterium exchange [protection]). Peptides are colored by the software automatically to display significant differences, determined either by a greater than 5% difference (less or more protection) in average deuterium uptake between the two states or by using the results of unpaired t-tests at each time point ($P < 0.05$ for any two time points or $P < 0.01$ for any single time point). Peptides with nonsignificant changes between the two states are colored gray. The exchange of the first two residues for any given peptide is not colored. Each peptide bar in the heatmap view displays the average Δ %D values, associated SD, and the charge state. In addition, overlapping peptides with similar differential deuterium exchange trends covering the same region are used to rule out data ambiguity. Bayesian analysis was performed natively in the HDXWorkbench application with the algorithms developed here[74]. Settings were the following: 4 runs per sample, 5000 steps, 20 bins, and 5 as the experimental error with 'Censor only' checked without scaling. Output from data rendering was transferred to ChimeraX (version 1.8) for generating data overlays onto prediction models.

These data have been deposited to the ProteomeXchange Consortium via the PRIDE[107] partner repository under the accession code PXD056400 for continuous labeling HDX-MS experiments.

Crosslinking mass spectrometry

Sample preparation. For DSSO (ThermoFisher, A33545) cross-linking reactions, PR was diluted to 5 µM in cross-linking buffer [20 mM Hepes (pH 7.5), 200 mM NaCl, 1 M Urea, 1 mM TCEP, and 5% glycerol] and incubated for 30 min at room temperature before initiating the cross-linking reaction. For multi-protein complexes, DNA was added, then PR, then SRC3, then p300, waiting 15 minutes between each sequential addition. The proteins were added at consistent molar ratios (PR:SRC3:p300:DNA; 2:1:1:1.5) as determined in this work, scaling each to PR at 5 µM concentration, total maximum protein concentration equal to 10 µM. The final incubation was performed for 30 minutes at room temperature. DSSO cross-linker was freshly dissolved in the cross-linking buffer to a final concentration of 150 mM before being added to the protein solution at a final concentration of 3 mM. The reaction was incubated at 25 °C for 45 min, then quenched by adding 1 µL of 2.0 M Tris-HCl (pH 8.0) and incubating for an additional 10 min at 25 °C. Control reactions were performed in parallel by DMSO addition in lieu of a chemical crosslinker. All cross-linking reactions were carried out in three replicates. The presence of cross-linked proteins was confirmed by comparing to the no-crosslink negative control samples using SDS-PAGE and Coomassie staining. The remaining cross-linked and non-crosslinked samples were separately pooled and precipitated using cold (−20 °C) acetone with overnight incubation. Dried protein pellets were resuspended in 12.5 µL of resuspension buffer [50 mM ammonium bicarbonate and 8 M urea (pH 8.0)]. ProteaseMAX (Promega, V5111) was added to a final concentration of 0.02%, and the solutions were mixed on an orbital shaker operating at 600 rpm for 5 min. After resuspension, 87.5 µL of digestion buffer [50 mM ammonium bicarbonate (pH 8.0)] was added. Protein solutions were digested using trypsin (Promega, V5280) at a ratio of 1:150 (w/w) (trypsin:protein) for 4 h at 37 °C, then digested overnight at room temperature using chymotrypsin (Promega, V1061) at a ratio of 1:150 (w/w) (chymotrypsin:protein). Peptides were acidified to a final concentration of 1% TFA and desalted using C18 ZipTip (Millipore Sigma, ZTC185096). Desalted peptides were dried using a vacuum centrifuge (SpeedVac, ThermoFisher). Dried peptides were resuspended in 20 µL of 0.1% TFA in water. Samples were frozen and stored at −20 °C until LC-MS analysis.

Liquid chromatography and mass spectrometry. A total of 250 ng of sample was injected (triplicate injections for cross-linked samples and duplicate injections for control samples) onto an UltiMate 3000 UHPLC system (Dionex, ThermoFisher Scientific). Peptides were trapped using an Acclaim PepMap C18 trapping column (ThermoFisher Scientific) using a load pump operating at 10 µL/min. Peptides were separated on a 200 cm µPAC C18 column (PharmaFluidics/ThermoFisher) using a linear gradient (1% solvent B for 4 min, 1 to 30% solvent B from 4 to 70 min, 30 to 55% solvent B from 70 to 90 min, 55 to 97% solvent B from 90 to 112 min, and isocratic at 97% solvent B from 112 to 120 min) at a flow rate of 800 nL/min. Gradient solvent A contained 0.1% formic acid, and solvent B contained 80% acetonitrile and 0.1% formic acid. LC eluate was interfaced to an Orbitrap Fusion Lumos Tribrid mass spectrometer (ThermoFisher Scientific) with a Nanospray Flex ion source (ThermoFisher

Scientific). For differential antagonist-bound PR samples, a FAIMS source was used with carrier gas of 4 L/min and compensation voltages of − 50, − 60, and − 75, based on published XL-MS data acquisition strategies[108]. The source voltage was set to 2 kV, and the S-Lens RF level was set to 30%. Agonist-bound PR crosslinks were identified using an MS2-MS3 acquisition method[109] with slight modifications. Full scans were recorded from mass/charge ratio (m/z) 150–1500 at a resolution of 60,000 in the Orbitrap mass analyzer. The automatic gain control (AGC) target value was set to 4E5, and the maximum injection time was set to 50 ms in the Orbitrap. MS2 scans were recorded at a resolution of 30,000 in the Orbitrap mass analyzer. Only precursors with charge states between 4 and 8 were selected for MS2 scans. The AGC target was set to 5E4, a maximum injection time of 150 ms, and an isolation width of 1.6 m/z. Collision-induced dissociation fragmentation energy was set to 25%. RU486 samples used a stepped, normalized higher energy collisional dissociation (HCD) fragmentation method with collision energies of 15, 30, and 45. The two most abundant reporter doublets from the MS2 scans with a charge state of 2 to 6, a 31.9721-Da mass difference, and a mass tolerance of ±10 parts per million (ppm) were selected for MS3 for all other samples. The MS3 scans were performed in the ion trap in rapid mode using higher-energy C-trap dissociation (HCD) fragmentation of 35% collision energy. The AGC target was set to 2E4, the maximum injection time was set to 200 ms, and the isolation width was set to 2.0 m/z.

Data analysis. To identify cross-linked peptides, Thermo *.raw files were imported into Proteome Discoverer 3.0 (ThermoFisher Scientific) and analyzed via XlinkX algorithm[110] using the MS2_MS3 workflow with the following parameters: MS1 mass tolerance, 10 ppm; MS2 mass tolerance, 20 ppm; MS3 mass tolerance, 0.5 Da; digestion: trypsin/chymotrypsin with four missed cleavages allowed; minimum peptide length: 4; variable modification: oxidation (M), DSSO (K, S, T, and Y), and hydrolyzed DSSO (K, S, T, and Y). FAIMS-enabled data was searched similarly but used the MS2 acquisition method in lieu of the MS2_MS3 method. The XlinkX/PD Validator node was used for cross-linked peptide validation with a 1% false discovery rate. Identified cross-links were further validated and quantified using Skyline (version 19.1)[111,112] by quantifying crosslink peptide intensity and comparing pairwise-ratios of the transition peak areas for cross-linked peptides using a two-tailed t-test within the group comparison node, performed natively, and similar to that described previously[113]. Cross-link spectral matches found in Proteome Discoverer were exported and converted to sequence spectrum list format using Excel (Microsoft). Cross-link peak areas were assessed using the MS1 full-scan filtering protocol for peaks within 8 min of the cross-link spectral match identification. Peak areas were assigned to the specified cross-linked peptide identification if the mass error was within 10 ppm of the theoretical mass, the isotope dot product was greater than 0.85, and the peak was not found in the non–cross-linked negative control samples. The isotope dot product compares the distribution of the measured MS1 signals against the theoretical isotope abundance distribution calculated based on the peptide sequence. Its value ranges between 0 and 1, where 1 indicates a perfect match[114]. Pairwise comparisons were made using the "MSstats" package implemented in Skyline to calculate relative fold changes and significance using linear mixed-effects models[115]. Significant change thresholds were defined as a log2 fold change less than − 1 or greater than 1 and $-\log_{10}$ P value greater than 1.3 (*P*-value less than 0.05). Visualization of proteins and cross-links was generated using xiView[116]. Volcano plots were reformatted using Skyline output data within R with the tidyverse and ggplot2 packages[117].

The data have been deposited to the ProteomeXchange Consortium via the PRIDE[107] partner repository with the dataset identifier PXD056360.

Structure prediction. PR models and combination PR:SRC3:p300 ternary models were generated using five independent runs with different seeds using the AlphaFold3.0 server[45]. The sequences provided were from the Uniprot P40601 isoforms for PR, Q9Y6Q9 for SRC3, and Q09472 for p300. The 32 bp canonical PRE was modeled after the PRE used for crystallization experiments with the PR DBD[1] (RCSB:2C7A). Top models from each independent run were opened and aligned in ChimeraX (version 1.8[118–120]). HDX-MS outputs were taken from HDXWorkbench[105] and overlayed onto the generated models. Top models were selected based on average HDXer[70] root mean square error (RMSE) values. HDXer was run using an automated server-based system to generate topology and gromacs files using the AMBER3.0 force fields. Topologies were then submitted to the server-based pipeline, and RMSE values were generated from the differences between predicted and experimental deuterium exchange values.

Reporting summary

Further information on research design is available in the Nature Portfolio Reporting Summary linked to this article.

Data availability

The XL-MS and HDX-MS raw data generated in this study have been deposited in the ProteomeXchange Consortium via the PRIDE partner repository under accession codes PXD056360 and PXD056400, respectively. The transcriptional response assay, mass spectrometry protein characterization, SEC-MALS, and MMS data generated in this study are provided in the Source Data file. Source Data have been placed at https://doi.org/10.6084/m9.figshare.28790798.

References

1. Roemer, S. C. et al. Structure of the progesterone receptor-deoxyribonucleic acid complex: novel interactions required for binding to half-site response elements. *Mol. Endocrinol.* **20**, 3042–3052 (2006).
2. Melvin, V. S. et al. The role of the C-terminal extension (CTE) of the estrogen receptor alpha and beta DNA binding domain in DNA binding and interaction with HMGB. *J. Biol. Chem.* **279**, 14763–14771 (2004).
3. Hill, K. K., Roemer, S. C., Churchill, M. E. A. & Edwards, D. P. Structural and functional analysis of domains of the progesterone receptor. *Mol. Cell. Endocrinol.* **348**, 418–429 (2012).
4. Grimm, S. L., Hartig, S. M. & Edwards, D. P. Progesterone receptor signaling mechanisms. *J. Mol. Biol.* **428**, 3831–3849 (2016).
5. Simons, S. S., Edwards, D. P. & Kumar, R. Minireview: Dynamic structures of nuclear hormone receptors: New promises and challenges. *Mol. Endocrinol.* **28**, 173–182 (2014).
6. Bland, R. Steroid hormone receptor expression and action in bone. *Clin. Sci.* **98**, 217–240 (2000).
7. Graham, J. D. & Clarke, C. L. Physiological action of progesterone in target tissues*. *Endocr. Rev.* **18**, 502–519 (1997).
8. Graham, J. D. & Clarke, C. L. Progesterone receptors - animal models and cell signaling in breast cancer: Expression and transcriptional activity of progesterone receptor A and progesterone receptor B in mammalian cells. *Breast Cancer Res.* **4**, 182–186 (2002).
9. Han, Y., Feng, H. L., Sandlow, J. I. & Haines, C. J. Comparing expression of progesterone and estrogen receptors in testicular tissue from men with obstructive and nonobstructive Azoospermia. *J. Androl.* **30**, 127–133 (2009).
10. Ozawa, H. Steroid hormones, their receptors and neuroendocrine system. *J. Nippon Med. Sch.* **72**, 316–325 (2005).
11. Tincello, D. G., Taylor, A. H., Spurling, S. M. & Bell, S. C. Receptor isoforms that mediate estrogen and progestagen action in the female lower urinary tract. *J. Urol.* **181**, 1474–1482 (2009).

12. Asavasupreechar, T. et al. Systemic distribution of progesterone receptor subtypes in human tissues. *J. Steroid Biochem. Mol. Biol.* **199**, 105599 (2020).
13. Mulac-Jericevic, B., Lydon, J. P., Demayo, F. J. & Conneely, O. M. Defective mammary gland morphogenesis in mice lacking the progesterone receptor B isoform. *Proc. Natl. Acad. Sci. USA* **100**, 9744–9749 (2003).
14. Fernandez-Valdivia, R. et al. Transcriptional response of the murine mammary gland to acute progesterone exposure. *Endocrinology* **149**, 6236–6250 (2008).
15. Aupperlee, M. D. & Haslam, S. Z. Differential hormonal regulation and function of progesterone receptor isoforms in normal adult mouse mammary gland. *Endocrinology* **148**, 2290–2300 (2007).
16. Zheng, Z.-H. et al. METTL3 is essential for normal progesterone signaling during embryo implantation via m6A-mediated translation control of progesterone receptor. *Proc. Natl. Acad. Sci. USA* **120**, https://doi.org/10.1073/pnas.2214684120 (2023).
17. Takimoto, G. S. et al. Functional properties of the N-terminal region of progesterone receptors and their mechanistic relationship to structure. *J. Steroid Biochem. Mol. Biol.* **85**, 209–219 (2003).
18. Lee, S. H., Yap, Y. H. Y., Lim, C. L., Woo, A. R. E. & Lin, V. C. L. Activation function 1 of progesterone receptor is required for mammary development and regulation of RANKL during pregnancy. *Sci. Rep.* **12**, https://doi.org/10.1038/s41598-022-16289-x (2022).
19. Pu, H., Wen, X., Luo, D. & Guo, Z. Regulation of progesterone receptor expression in endometriosis, endometrial cancer, and breast cancer by estrogen, polymorphisms, transcription factors, epigenetic alterations, and ubiquitin-proteasome system. *J. Steroid Biochem. Mol. Biol.* **227**, 106199 (2023).
20. Meyer, M. E., Quirin-Stricker, C., Lerouge, T., Bocquel, M. T. & Gronemeyer, H. A limiting factor mediates the differential activation of promoters by the human progesterone receptor isoforms. *J. Biol. Chem.* **267**, 10882–10887 (1992).
21. Tung, L. et al. Progesterone receptors (PR)-B and -A regulate transcription by different mechanisms: AF-3 exerts regulatory control over coactivator binding to PR-B. *Mol. Endocrinol.* **20**, 2656–2670 (2006).
22. Vegeto, E. et al. Human progesterone receptor A form is a cell- and promoter-specific repressor of human progesterone receptor B function. *Mol. Endocrinol.* **7**, 1244–1255 (1993).
23. Obr, A. E. & Edwards, D. P. The biology of progesterone receptor in the normal mammary gland and in breast cancer. *Mol. Cell. Endocrinol.* **357**, 4–17 (2012).
24. Mote, P. A., Balleine, R. L., Mcgowan, E. M. & Clarke, C. L. Colocalization of progesterone receptors A and B by dual immunofluorescent histochemistry in human endometrium during the menstrual cycle1. *J. Clin. Endocrinol. Metab.* **84**, 2963–2971 (1999).
25. Mote, P. A. et al. Overlapping and distinct expression of progesterone receptors A and B in mouse uterus and mammary gland during the estrous cycle. *Endocrinology* **147**, 5503–5512 (2006).
26. Merlino, A. A. et al. Nuclear progesterone receptors in the human pregnancy myometrium: Evidence that parturition involves functional progesterone withdrawal mediated by increased expression of progesterone receptor-A. *J. Clin. Endocrinol. Metab.* **92**, 1927–1933 (2007).
27. Li, W. N., Dickson, M. J., DeMayo, F. J. & Wu, S. P. The role of progesterone receptor isoforms in the myometrium. *J. Steroid Biochem. Mol. Biol.* **224**, 106160 (2022).
28. Richer, J. K. et al. Differential gene regulation by the two progesterone receptor isoforms in human breast cancer cells. *J. Biol. Chem.* **277**, 5209–5218 (2002).
29. Mote, P. A., Bartow, S., Tran, N. & Clarke, C. L. Loss of co-ordinate expression of progesterone receptors A and B is an early event in breast carcinogenesis. *Breast Cancer Res. Treat.* **72**, 163–172 (2002).
30. Graham, J. D. et al. Characterization of progesterone receptor A and B expression in human breast cancer1. *Cancer Res.* **55**, 5063–5068 (1995).
31. Hopp, T. A. et al. Breast cancer patients with progesterone receptor PR-A-Rich tumors have poorer disease-free survival rates. *Clin. Cancer Res.* **10**, 2751–2760 (2004).
32. Truong, T. H. et al. Phosphorylated progesterone receptor isoforms mediate opposing stem cell and proliferative breast cancer cell fates. *Endocrinology* **160**, 430–446 (2019).
33. Pathiraja, T. N. et al. Progesterone receptor isoform-specific promoter methylation: Association of PRA promoter methylation with worse outcome in breast cancer patients. *Clin. Cancer Res.* **17**, 4177–4186 (2011).
34. Graham, J. D. et al. Altered progesterone receptor isoform expression remodels progestin responsiveness of breast cancer cells. *Mol. Endocrinol.* **19**, 2713–2735 (2005).
35. Attia, G. R. et al. Progesterone receptor isoform A but not B is expressed in endometriosis. *J. Clin. Endocrinol. Metab.* **85**, 2897–2902 (2000).
36. Giangrande, P. H., A. Kimbrel, E., Edwards, D. P. & Mcdonnell, D. P. The opposing transcriptional activities of the two isoforms of the human progesterone receptor are due to differential cofactor binding. *Mol. Cell. Biol.* **20**, 3102–3115 (2000).
37. Singhal, H. et al. Progesterone receptor isoforms, agonists and antagonists differentially reprogram estrogen signaling. *Oncotarget* **9**, 4282–4300 (2018).
38. Lim, C. S. et al. Differential localization and activity of the A- and B-forms of the human progesterone receptor using green fluorescent protein chimeras. *Mol. Endocrinol.* **13**, 366–375 (1999).
39. Boonyaratanakornkit, V. et al. The role of extranuclear signaling actions of progesterone receptor in mediating progesterone regulation of gene expression and the cell cycle. *Mol. Endocrinol.* **21**, 359–375 (2007).
40. Williams, S. P. & Sigler, P. B. Atomic structure of progesterone complexed with its receptor. *Nature* **393**, 392–396 (1998).
41. Raaijmakers, H. C. A., Versteegh, J. E. & Uitdehaag, J. C. M. The X-ray Structure of RU486 bound to the progesterone receptor in a destabilized agonistic conformation. *J. Biol. Chem.* **284**, 19572–19579 (2009).
42. Petit-Topin, I. et al. Molecular determinants of the recognition of ulipristal acetate by oxo-steroid receptors. *J. Steroid Biochem. Mol. Biol.* **144**, 427–435 (2014).
43. Yu, X. et al. Spatial definition of the human progesterone receptor-B transcriptional complex. *iScience* **25**, 105321 (2022).
44. Liu, Z., Wong, J., Tsai, S. Y., Tsai, M.-J. & O'Malley, B. W. Sequential recruitment of steroid receptor coactivator-1 (SRC-1) and p300 enhances progesterone receptor-dependent initiation and reinitiation of transcription from chromatin. *Proc. Natl. Acad. Sci.* **98**, 12426–12431 (2001).
45. Yi, P. et al. Structural and functional impacts of ER coactivator sequential recruitment. *Mol. Cell* **67**, 733–743 (2017).
46. Zhang, Z. & Smith, D. L. Determination of amide hydrogen exchange by mass spectrometry: A new tool for protein structure elucidation. *Protein Sci.* **2**, 522–531 (1993).
47. Bai, Y., Milne, J. S., Mayne, L. & Englander, S. W. Primary structure effects on peptide group hydrogen exchange. *Proteins Struct. Funct. Genet.* **17**, 75–86 (1993).
48. Chalmers, M. J. et al. Probing protein ligand interactions by automated hydrogen/deuterium exchange mass spectrometry. *Anal. Chem.* **78**, 1005–1014 (2006).
49. Wales, T. E. & Engen, J. R. Hydrogen exchange mass spectrometry for the analysis of protein dynamics. *Mass Spectrom. Rev.* **25**, 158–170 (2006).

50. Zheng, J., Strutzenberg, T., Pascal, B. D. & Griffin, P. R. Protein dynamics and conformational changes explored by hydrogen/deuterium exchange mass spectrometry. *Curr. Opin. Struct. Biol.* **58**, 305–313 (2019).
51. Hofmann, T., Fischer, A. W., Meiler, J. & Kalkhof, S. Protein structure prediction guided by crosslinking restraints – A systematic evaluation of the impact of the crosslinking spacer length. *Methods* **89**, 79–90 (2015).
52. Chavez, J. D. et al. Chemical crosslinking mass spectrometry analysis of protein conformations and supercomplexes in heart tissue. *Cell Syst.* **6**, 136–141 (2018).
53. Schneider, M., Belsom, A. & Rappsilber, J. Protein tertiary structure by crosslinking/mass spectrometry. *Trends Biochem. Sci.* **43**, 157–169 (2018).
54. Brodie, N. I., Sarpe, V., Crowder, D. A. & Schriemer, D. All-in-one pseudo-MS^3 method for the analysis of gas-phase cleavable protein crosslinking reactions. *J. Am. Soc. Mass Spectrom.* **34**, 2146–2155 (2023).
55. Elliston, J. F., Beekman, J. M., Tsai, S. Y., O'Malley, B. W. & Tsai, M. J. Hormone activation of baculovirus expressed progesterone receptors. *J. Biol. Chem.* **267**, 5193–5198 (1992).
56. Beck, C. A., Zhang, Y., Altmann, M., Weigel, N. L. & Edwards, D. P. Stoichiometry and site-specific phosphorylation of human progesterone receptor in native target cells and in the baculovirus expression system. *J. Biol. Chem.* **271**, 19546–19555 (1996).
57. Christensen, K. et al. Characterization and functional properties of the A and B forms of human progesterone receptors synthesized in a baculovirus system. *Mol. Endocrinol.* **5**, 1755–1770 (1991).
58. Wardell, S. E., Kwok, S. C., Sherman, L., Hodges, R. S. & Edwards, D. P. Regulation of the amino-terminal transcription activation domain of progesterone receptor by a cofactor-induced protein folding mechanism. *Mol. Cell. Biol.* **25**, 8792–8808 (2005).
59. Kumar, R. et al. Regulation of the structurally dynamic N-terminal domain of progesterone receptor by protein-induced folding. *J. Biol. Chem.* **288**, 30285–30299 (2013).
60. Goswami, D. et al. Influence of domain interactions on conformational mobility of the progesterone receptor detected by hydrogen/deuterium exchange mass spectrometry. *Structure* **22**, 961–973 (2014).
61. Rayasam, G. V. et al. Ligand-specific dynamics of the progesterone receptor in living cells and during chromatin remodeling In vitro. *Mol. Cell. Biol.* **25**, 2406–2418 (2005).
62. Zhang, Y. et al. Phosphorylation of human progesterone receptor by cyclin-dependent kinase 2 on three sites that are authentic basal phosphorylation sites in vivo. *Mol. Endocrinol.* **11**, 823–832 (1997).
63. Schmidt, T. G. & Skerra, A. The Strep-tag system for one-step purification and high-affinity detection or capturing of proteins. *Nat. Protoc.* **2**, 1528–1535 (2007).
64. Zhang, Y., Beck, C. A., Poletti, A., Edwards, D. P. & Weigel, N. L. Identification of a group of Ser-Pro motif hormone-inducible phosphorylation sites in the human progesterone receptor. *Mol. Endocrinol.* **9**, 1029–1040 (1995).
65. Lee, C.-R., Park, Y.-H., Min, H., Kim, Y.-R. & Seok, Y.-J. Determination of protein phosphorylation by polyacrylamide gel electrophoresis. *J. Microbiol.* **57**, 93–100 (2019).
66. Liu, L. L., Wang, L., Zonderman, J., Rouse, J. C. & Kim, H. Y. Automated, high-throughput infrared spectroscopy for secondary structure analysis of protein biopharmaceuticals. *J. Pharm. Sci.* **109**, 3223–3230 (2020).
67. Ivancic, V. A., Lombardo, H. L., Ma, E., Wikstrom, M. & Batabyal, D. Advancing secondary structure characterization of monoclonal antibodies using microfluidic modulation spectroscopy. *Anal. Biochem.* **646**, 114629 (2022).
68. Some, D., Amartely, H., Tsadok, A. & Lebendiker, M. Characterization of proteins by size-exclusion chromatography coupled to multi-angle light scattering (SEC-MALS). *J. Vis. Exp.* **120**, https://doi.org/10.3791/59615 (2019).
69. Abramson, J. et al. Accurate structure prediction of biomolecular interactions with AlphaFold 3. *Nature* **630**, 493–500 (2024).
70. Lee, P. S. et al. Interpreting hydrogen-deuterium exchange experiments with molecular simulations: Tutorials and applications of the HDXer ensemble reweighting software [Article v1.0]. *Living J. Comput. Mol. Sci.* **3**, https://doi.org/10.33011/livecoms.3.1.1521 (2021).
71. Heery, D. M., Hoare, S., Hussain, S., Parker, M. G. & Sheppard, H. Core LXXLL Motif sequences in CREB-binding protein, SRC1, and RIP140 define affinity and selectivity for steroid and retinoid receptors. *J. Biol. Chem.* **276**, 6695–6702 (2001).
72. Kattoula, S. R. & Baker, M. E. Structural and evolutionary analysis of the co-activator binding domain in vertebrate progesterone receptors. *J. Steroid Biochem. Mol. Biol.* **141**, 7–15 (2014).
73. Ding, X. F. et al. Nuclear receptor-binding sites of coactivators glucocorticoid receptor interacting protein 1 (GRIP1) and steroid receptor coactivator 1 (SRC-1): multiple motifs with different binding specificities. *Mol. Endocrinol.* **12**, 302–313 (1998).
74. Saltzberg, D. J. et al. A residue-resolved bayesian approach to quantitative interpretation of hydrogen–deuterium exchange from mass spectrometry: Application to characterizing protein–ligand interactions. *J. Phys. Chem. B* **121**, 3493–3501 (2017).
75. Aarts, M. T., Wagner, M., Van Der Wal, T., Van Boxtel, A. L. & Van Amerongen, R. A molecular toolbox to study progesterone receptor signaling. *J. Mammary Gland Biol. Neoplasia* **28**, https://doi.org/10.1007/s10911-023-09550-0 (2023).
76. Zhou, X. E. et al. Identification of SRC3/AIB1 as a preferred coactivator for hormone-activated androgen receptor. *J. Biol. Chem.* **285**, 9161–9171 (2010).
77. Le Douarin, B. et al. A possible involvement of TIF1 alpha and TIF1 beta in the epigenetic control of transcription by nuclear receptors. *EMBO J.* **15**, 6701–6715 (1996).
78. Edwards, D. P. et al. Progesterone receptor and the mechanism of action of progesterone antagonists. *J. Steroid Biochem. Mol. Biol.* **53**, 449–458 (1995).
79. Leonhardt, S. A., Altmann, M. & Edwards, D. P. Agonist and antagonists induce homodimerization and mixed ligand heterodimerization of human progesterone receptors in vivo by a mammalian two-hybrid assay. *Mol. Endocrinol.* **12**, 1914–1930 (1998).
80. Allan, G. F. et al. Hormone and antihormone induce distinct conformational changes which are central to steroid receptor activation. *J. Biol. Chem.* **267**, 19513–19520 (1992).
81. Weigel, N. L. et al. Ligands induce conformational changes in the carboxyl-terminus of progesterone receptors which are detected by a site-directed antipeptide monoclonal antibody. *Mol. Endocrinol.* **6**, 1585–1597 (1992).
82. Madauss, K. P. et al. A structural and in vitro characterization of asoprisnil: a selective progesterone receptor modulator. *Mol. Endocrinol.* **21**, 1066–1081 (2007).
83. Jacobsen, B. M., Richer, J. K., Schittone, S. A. & Horwitz, K. B. New human breast cancer cells to study progesterone receptor isoform ratio effects and ligand-independent gene regulation. *J. Biol. Chem.* **277**, 27793–27800 (2002).
84. Brayman, M. J. et al. Progesterone receptor isoforms A and B differentially regulate MUC1 expression in uterine epithelial cells. *Mol. Endocrinol.* **20**, 2278–2291 (2006).
85. Tung, L., Mohamed, M. K., Hoeffler, J. P., Takimoto, G. S. & Horwitz, K. B. Antagonist-occupied human progesterone B-receptors activate transcription without binding to progesterone response elements and are dominantly inhibited by A-receptors. *Mol. Endocrinol.* **7**, 1256–1265 (1993).

86. Tetel, M. J., Giangrande, P. H., Leonhardt, S. A., Mcdonnell, D. P. & Edwards, D. P. Hormone-dependent interaction between the amino- and carboxyl-terminal domains of progesterone receptor in vitro and in vivo. *Mol. Endocrinol.* **13**, 910–924 (1999).
87. Bain, D. L., Franden, M. A., Mcmanaman, J. L., Takimoto, G. S. & Horwitz, K. B. The N-terminal region of the human progesterone A-receptor. *J. Biol. Chem.* **275**, 7313–7320 (2000).
88. Bain, D. L., Franden, M. A., Mcmanaman, J. L., Takimoto, G. S. & Horwitz, K. B. The N-terminal region of human progesterone B-receptors. *J. Biol. Chem.* **276**, 23825–23831 (2001).
89. Beato, M. & Vicent, G. P. Impact of chromatin structure and dynamics on PR signaling. The initial steps in hormonal gene regulation. *Mol. Cell. Endocrinol.* **357**, 37–42 (2012).
90. Moody, A. D., Miura, M. T., Connaghan, K. D. & Bain, D. L. Thermodynamic dissection of estrogen receptor–promoter interactions reveals that steroid receptors differentially partition their self-association and promoter binding energetics. *Biochemistry* **51**, 739–749 (2012).
91. Noddings, C. M., Wang, R. Y.-R., Johnson, J. L. & Agard, D. A. Structure of Hsp90–p23–GR reveals the Hsp90 client-remodelling mechanism. *Nature* **601**, 465–469 (2022).
92. Noddings, C. M., Johnson, J. L. & Agard, D. A. Cryo-EM reveals how Hsp90 and FKBP immunophilins co-regulate the glucocorticoid receptor. *Nat. Struct. Mol. Biol.* **30**, 1867–1877 (2023).
93. Severson, T. M. et al. Characterizing steroid hormone receptor chromatin binding landscapes in male and female breast cancer. *Nat. Commun.* **9**, 482 (2018).
94. Le Dily, F. et al. Hormone-control regions mediate steroid receptor–dependent genome organization. *Genome Res.* **29**, 29–39 (2019).
95. Tettey, T. T., Rinaldi, L. & Hager, G. L. Long-range gene regulation in hormone-dependent cancer. *Nat. Rev. Cancer* **23**, 657–672 (2023).
96. Leo, C. & Chen, J. D. The SRC family of nuclear receptor coactivators. *Gene* **245**, 1–11 (2000).
97. Chauchereau, A., Amazit, L., Quesne, M., Guiochon-Mantel, A. & Milgrom, E. Sumoylation of the progesterone receptor and of the steroid receptor coactivator SRC-1. *J. Biol. Chem.* **278**, 12335–12343 (2003).
98. Han, S. J. et al. Steroid receptor coactivator (SRC)-1 and SRC-3 differentially modulate tissue-specific activation functions of the progesterone receptor. *Mol. Endocrinol.* **20**, 45–55 (2006).
99. Song, X. et al. Steroid receptor coactivator-3 (SRC-3/AIB1) as a novel therapeutic target in triple negative breast cancer and its inhibition with a phospho-bufalin prodrug. *PLOS ONE* **10**, e0140011 (2015).
100. Molenda-Figueira, H. A. et al. Steroid receptor coactivator-1 from brain physically interacts differentially with steroid receptor subtypes. *Endocrinology* **149**, 5272–5279 (2008).
101. Wardell, S. E., Narayanan, R., Weigel, N. L. & Edwards, D. P. Partial agonist activity of the progesterone receptor antagonist RU486 mediated by an amino-terminal domain coactivator and phosphorylation of serine^{400}. *Mol. Endocrinol.* **24**, 335–345 (2010).
102. Leo, J. C. L. & Lin, V. C. L. The activities of progesterone receptor isoform A and B are differentially modulated by their ligands in a gene-selective manner. *Int. J. Cancer* **122**, 230–243 (2008).
103. Allard, S. T. M. *Bioluminescent Reporter Genes*. (2008).
104. Savitzky, A. & Golay, M. J. E. Smoothing and differentiation of data by simplified least squares procedures. *Anal. Chem.* **36**, 1627–1639 (1964).
105. Pascal, B. D. et al. HDX Workbench: Software for the analysis of H/D exchange MS data. *J. Am. Soc. Mass Spectrom.* **23**, 1512–1521 (2012).
106. Keppel, T. R. & Weis, D. D. Mapping residual sructure in intrinsically disordered proteins at residue resolution using millisecond hydrogen/deuterium exchange and residue averaging. *J. Am. Soc. Mass Spectrom.* **26**, 547–554 (2015).
107. Perez-Riverol, Y. et al. The PRIDE database and related tools and resources in 2019: improving support for quantification data. *Nucleic Acids Res.* **47**, D442–D450 (2019).
108. Schnirch, L. et al. Expanding the depth and sensitivity of cross-link identification by differential ion mobility using high-field asymmetric waveform ion mobility spectrometry. *Anal. Chem.* **92**, 10495–10503 (2020).
109. Liu, F., Lössl, P., Scheltema, R., Viner, R. & Heck, A. J. R. Optimized fragmentation schemes and data analysis strategies for proteome-wide cross-link identification. *Nat. Commun.* **8**, 15473 (2017).
110. Liu, F., Rijkers, D. T. S., Post, H. & Heck, A. J. R. Proteome-wide profiling of protein assemblies by cross-linking mass spectrometry. *Nat. Methods* **12**, 1179–1184 (2015).
111. Pino, L. K. et al. The Skyline ecosystem: Informatics for quantitative mass spectrometry proteomics. *Mass Spectrom. Rev.* **39**, 229–244 (2020).
112. MacLean, B. et al. Skyline: an open source document editor for creating and analyzing targeted proteomics experiments. *Bioinformatics* **26**, 966–968 (2010).
113. Chen, Z. & Rappsilber, J. A generic solution for quantifying cross-linked peptides using software Skyline. *Protoc. Exch.* https://doi.org/10.1038/protex.2018.001 (2018).
114. Chen, Z. A. & Rappsilber, J. Quantitative cross-linking/mass spectrometry to elucidate structural changes in proteins and their complexes. *Nat. Protoc.* **14**, 171–201 (2019).
115. Choi, M. et al. MSstats: an R package for statistical analysis of quantitative mass spectrometry-based proteomic experiments. *Bioinformatics* **30**, 2524–2526 (2014).
116. Combe, C. W., Fischer, L. & Rappsilber, J. xiNET: Cross-link Network Maps With Residue Resolution. *Mol. Cell. Proteom.* **14**, 1137–1147 (2015).
117. Wickham, H. et al. Welcome to the Tidyverse. *J. Open Source Softw.* **4**, https://doi.org/10.21105/joss.01686 (2019).
118. Goddard, T. D. et al. UCSF ChimeraX: Meeting modern challenges in visualization and analysis. *Protein Sci.* **27**, 14–25 (2018).
119. Pettersen, E. F. et al. UCSF ChimeraX: Structure visualization for researchers, educators, and developers. *Protein Sci.* **30**, 70–82 (2021).
120. Meng, E. C. et al. UCSF ChimeraX: Tools for structure building and analysis. *Protein Science* **32**, https://doi.org/10.1002/pro.4792 (2023).

Acknowledgements

This work was supported by NIH-NCI R01 (CA263574) to MPIs, P.R.G., R.K., and D.P.E. The authors acknowledge the expert assistance of the Recombinant Protein Production and Characterization Core (RPPCC) for expression of recombinant proteins in the baculovirus insect cell system and the Mass Spectrometry Proteomics (MSPC) Core for amino acid sequencing and phosphorylation analysis of recombinant proteins. The RPPCC and MSPC at BCM are supported by the NCI Cancer Center Support Grant (P30 CA125123) of the Dan L Duncan Comprehensive Cancer Center, and the MSPC is additionally supported by a CPRIT (Cancer Prevention and Research Institute of Texas) Core Facility Support Award (RP210227). Additional support is from NIH S10 Shared Instrument Grant (1S10OD030276) to JCF for the SEC-MALS instruments.

Author contributions

P.R.G. and M.D.M. conceptualized progesterone receptor structural proteomics and mutagenesis studies. M.D.M. designed, performed, and analyzed the structural proteomics (HDX-MS and XL-MS) and transcriptional response data, including the preparation of site-directed mutants and all visualizations provided. D.P.E. provided up-front

experimental design and oversight of recombinant protein expression and purifications, quality control of purified products, and conditions for assembly of complexes for XL-MS and HDX-MS experiments. P.T. prepared baculovirus vectors and expressed recombinant proteins in scale-up Sf9 insect cell cultures. J.F. performed experimental design of SEC-MALS and MMS biophysical analyses, presentation, and analysis of biophysical data, and contributed to the writing of the manuscript. M.W. optimized purification procedures and performed purifications and quality control analysis of full-length proteins in the study. P.T. performed purification of proteins, SEC-MALS analysis of protein-DNA complexes, MMS analysis of secondary protein structure, and developed methods for analysis and presentation of MMS data. A.J. performed mass spectrometry sequencing and phosphosite analysis of purified proteins. A.M. developed methods for mass spectrometry analysis of protein phosphosites, performed analysis of data, and contributed to writing the manuscript. R.V.A. and B.D.P. performed Bayesian analysis of HDX-MS data and carried out HDXer analysis on AlphaFold3 structures from HDX-MS data. R.K., D.P.E., and P.R.G. supervised and directed this project. D.P.E., M.D.M., R.K., and P.R.G. contributed significantly to writing the manuscript. All authors contributed to editing the final version of this manuscript.

Competing interests

B.D.P. and R.V.A. are employed by Omics Informatics, a company that provides HDX-MS analysis software (HDX Workbench) free to academics. The remaining authors declare no competing interests.

Additional information

Supplementary information The online version contains supplementary material available at https://doi.org/10.1038/s41467-025-59458-y.

Correspondence and requests for materials should be addressed to Patrick R. Griffin.

Peer review information *Nature Communications* thanks the anonymous reviewer(s) for their contribution to the peer review of this work. A peer review file is available.